Sensor and Simulation Notes

Note 380

June 1995

Compact Ultra-Short Pulse Fuzing Antenna Design and Measurements

Everett G. Farr
Farr Research

Charles A. Frost
Pulse Power Physics

Abstract

We consider here antennas that could be useful as part of a fuze radar for penetrating munitions. The concept requires radiating an ultra-short pulse using an antenna with maximum gain and a compact design. Both lens and reflector Impulse Radiating Antennas (IRAs) are recommended as suitable candidates for this purpose. We summarize the properties of these antennas, and we describe two measurement techniques for determining their characteristics. The first technique involves a single antenna and a large planar reflector; the second technique uses two identical antennas. We have built a pair of reflector IRAs with $F/D = 0.25$ and diameter = 46 cm, and measurements were performed using both of the techniques described. In addition, since propagation issues will also be important to such a radar system, we sketch out some of the available analytical and numerical models of pulse propagation through frequency-dependent dielectric media. Finally, we suggest experimental configurations for measuring these propagation characteristics.

I. Introduction

The purpose of this project is to analyze and test some candidate antennas which could be useful for Ultra-Short Pulse fuzing applications. Such antennas would be used to locate underground targets for penetrating munitions. The general goal here is to design and test small antennas that have the highest possible gain, and which can radiate a pulse less than 100 ps in duration.

We begin by describing three reasonable candidate antenna designs, the reflector Impulse Radiating Antenna (IRA) the lens IRA, and the solid dielectric lens IRA. We provide estimates of their response, and we show how to use their characteristics in an antenna equation. We describe two methods for measuring the performance of these antennas. We provide signal processing algorithms for extracting the antenna characteristic from the measured data. Two copies of a reflector IRA were constructed and tested using the algorithms and experiments proposed here. Satisfactory agreement was found between theory and measurement.

Finally, we describe how one might measure the dielectric properties of various materials, such as soil, sand, and concrete. We also outline some basic analytic and numerical techniques for calculating the attenuation of short pulses as they propagate through these media. We begin now with a description of the candidate antennas.

II. Candidate Antennas

If one is to radiate a short pulse into the earth, one would normally want to have a planar phase front, in order to achieve optimal gain for a given aperture size. We consider here three antennas capable of radiating a fast pulse with a planar phase front. They include a reflector Impulse Radiating antenna (IRA) [1,2], a lens IRA[2], and a solid dielectric lens IRA. We consider first the reflector IRA.

A. Reflector IRA

The reflector IRA consists of a paraboloidal reflector fed by a conical TEM feed. An example of such an antenna is shown in Figure 2.1, along with an example of the expected radiated field when driven by a smooth step-function voltage with a fast risetime. The feed arms are normally flat plates that lie in the vertical plane, in order to reduce feed blockage. The feed impedance of a single pair of arms is typically 400 Ω.

Instead of a using just a single pair of arms, one would normally want to include a second pair of arms in the horizontal plane (Figure 2.2). This second pair of arms does not disturb the field of the first pair, but it has the effect of reducing the input impedance of the antenna from 400 Ω to 200 Ω. The dominant radiated field is then polarized at an angle of 45 degrees to the vertical, as shown in Figure 2.2. Note that if the impedance of the feed cable is 50 Ω, then one can build a balun that converts a 50 Ω impedance to a 200 Ω impedance with standard balun designs.

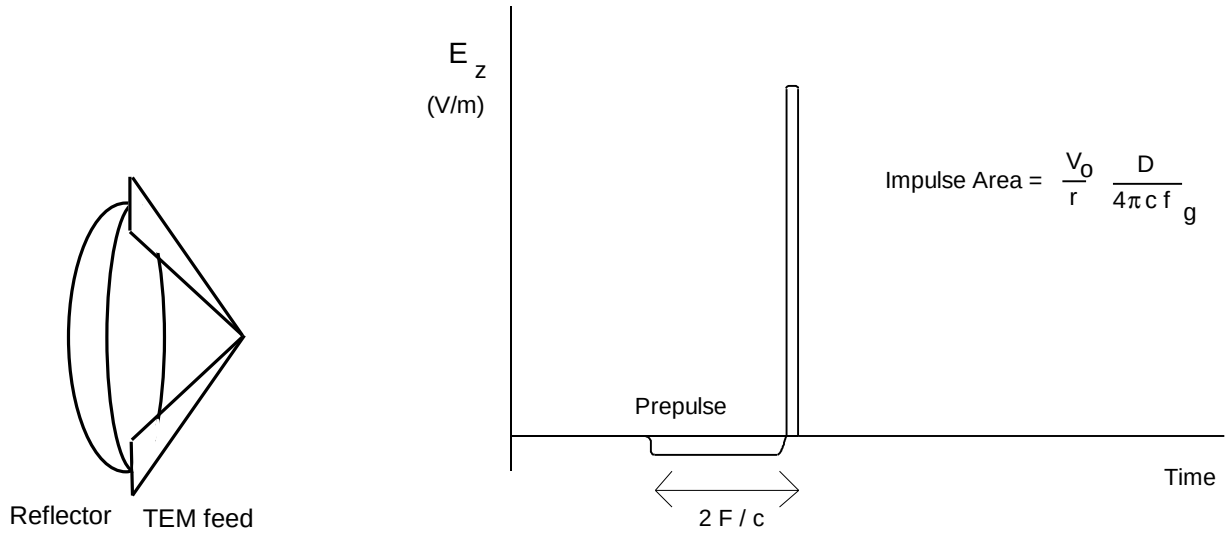

Figure 2.1. An example of a reflector IRA (left) and the radiated electric field on boresite when the antenna is driven by a fast, smooth step-function voltage (right).

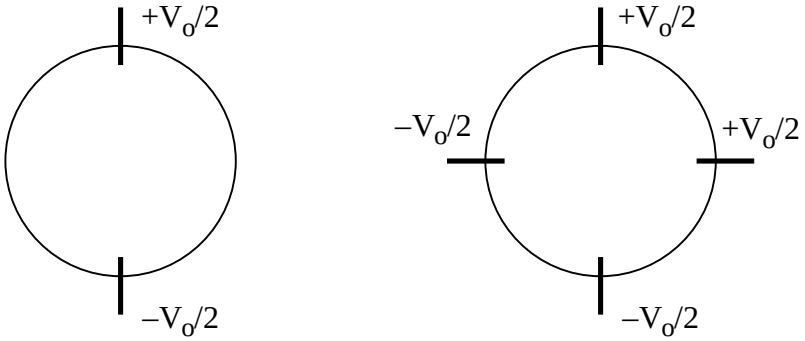

Figure 2.2. Reflector IRA configurations with two and four arms.

An approximate theory for the radiated field is well established for dominant polarization, when the observer is on boresight and in the far field. We assume here we drive a single pair of arms. If a second pair of arms is used, it is trivial to add their effect by superposition. The radiated field for a single pair of arms is approximately [1,2]

$$E(r,t) = \frac{D}{4p\,c\,f_g\,r}\left[\frac{dV(t-2F/c)}{dt} - \frac{c}{2F}\left[V(t)-V(t-2F/c)\right]\right] \tag{2.1}$$

where the feed impedance of a single pair of arms is expressed as f_g, where $f_g = Z_{feed}/Z_o$, and Z_o=376.727 Ω is the impedance of free space. Furthermore, D is the reflector diameter, F is the focal length of the reflector, and r is the distance out the to the observer. This expression is approximately valid for feed impedances of 400 Ω or greater for a single pair of arms. It will become convenient later to express this as a convolution of an antenna function with the derivative of the driving voltage. Thus, we have

$$\begin{aligned} E(r,t) &= \frac{1}{2p\,c\,f_g\,r}\,h(t) \circ \frac{dV_{inc}(t)}{dt} \\ h(t) &= \frac{D}{2}\left[\,d_a(t-2F/c) - \frac{c}{2F}\left[u(t)-u(t-2F/c)\right]\right] \end{aligned} \tag{2.2}$$

where $d_a(t)$ is an approximation to the Dirac delta function, $u(t)$ is the Heaviside step function and the "○" operator indicates a convolution. The approximate delta function becomes a true delta function in the limit as the distance from the antenna to the observer approaches infinity. It will be seen later that the $h(t)$ function for the IRA (or any antenna) is sufficient to specify its behavior in either transmission or reception. Note the very simple form for $h(t)$ for the reflector IRA.

It will also be useful to provide information concerning how to design the feed arms to achieve a given feed impedance. We define here three angles which must be specified, as shown in Figure 2.3. The angle b is determined simply by the F/D ratio of the parabola. If we define $f_d = F/D$, then we have from the equation of a parabola

$$b = \arctan\left(\frac{1}{2f_d - 1/(8f_d)}\right) \tag{2.3}$$

Furthermore, the feed impedance of TEM feed is [3]

$$f_g = \frac{K(m)}{K(1-m)} \tag{2.4}$$

where $K(m)$ is the complete elliptic integral of the first kind. If one wants a certain feed impedance, one must solve the above equation for m. For the usual case of the feed impedance being 400 Ω, we have m=0.565291. Having solved for m and b, one then finds the remaining angles as [3]

$$\begin{aligned} b_1 &= 2\arctan\left[m^{1/4}\tan(b/2)\right] \\ b_2 &= 2\arctan\left[m^{-1/4}\tan(b/2)\right] \end{aligned} \tag{2.5}$$

This completely specifies all the relevant angles for the feed.

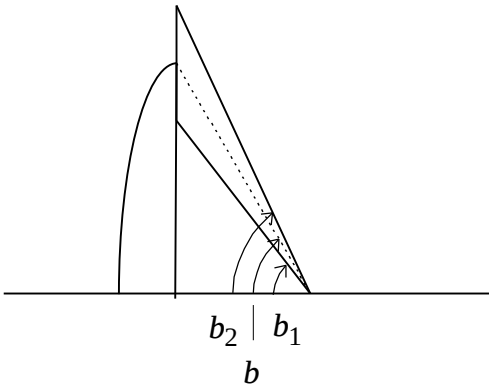

Figure 2.3. Angles for specifying the feed arm configuration.

B. Lens IRA

A second candidate antenna for the present application is a lens IRA. This consists of a TEM horn made out of sections of a circular cone, with a lens in front to flatten the phase front. A sketch of the antenna is shown in Figure 2.4, along with an approximate radiated field on boresight.

A lens IRA can have both advantages and disadvantages over a reflector IRA, depending on the situation. On the one hand, there is no feed blockage with a lens IRA. On the other hand, lenses can be quite heavy if the aperture is large. For the present application, the aperture will not be large. However, the lens is still somewhat cumbersome (and expensive) to build. A parabolic reflector with the correct specifications is much easier to obtain. For this reason, our measurements for this project concentrate on the reflector design. We provide here design data for the lens design since it may be needed for later work.

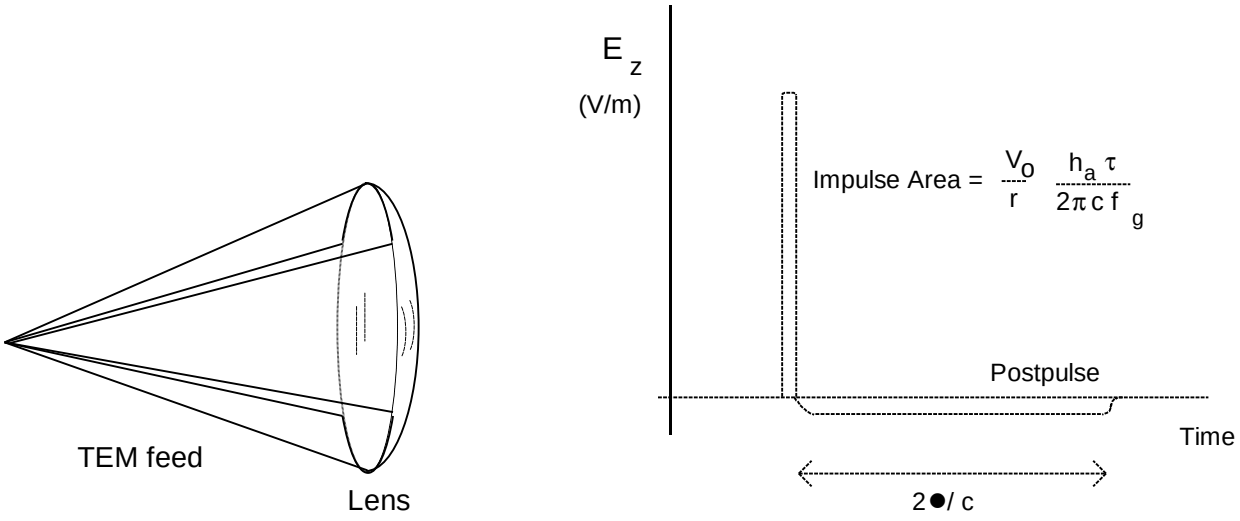

Figure 2.4. A lens IRA (left), and a typical radiated field when the antenna is driven by a fast, smooth step-function voltage (right).

An approximate theory of operation for a lens IRA is available. The radiated field on boresight in the far field is [4]

$$E(r,t) = \frac{h_a\ t}{2p\ c\ f_g\ r}\left[\frac{dV(t)}{dt} - \frac{c}{2\ell}\left[V(t) - V(t - 2\ell / c)\right]\right]$$
$$t = \frac{4\sqrt{e_r}}{\left(1+\sqrt{e_r}\right)^2} \qquad (2.6)$$

where ℓ is the length of the horn, r is the distance out to the observer, and h_a is an effective height function that depends upon feed impedance (f_g). For optimal radiation, Z_{feed} is $Z_o/2 = 377/2\ \Omega$. At this feed impedance, each arm of the TEM horn has an angular width of 90 degrees, and $h_a \sim 0.85 \times$ radius of aperture. Note also that t is the voltage transmission coefficient through the lens. For $e_r = 2.2$ (the dielectric constant of polyethylene), $t = 0.96$, so there is little loss in transmission through the lens.

Again, it is useful to convert the above expression to a convolution operator. Thus we have

$$E(r,t) = \frac{1}{2\pi c f_g r} h(t) \circ \frac{dV_{inc}(t)}{dt}$$
$$h(t) = h_a t \left[d_a(t) - \frac{c}{2\ell}\left[u(t) - u(t - 2\ell / c)\right] \right] \quad (2.7)$$

where $V_{inc}(t)$ is the incident voltage launched across the plates. Note the very strong similarity between the $h(t)$ functions for the lens IRA (above) and for the reflector IRA (eqn. 2.2).

C. Solid Dielectric Lens IRA

A third antenna design, the solid dielectric lens IRA is also being considered. It is similar to a lens IRA, with the exception that all the material between the plates is a solid dielectric. The end is terminated as before in a lens that maintains a flat phase front. An example of such an antenna is shown in Figure 2.5, along with a sample of its expected output.

This antenna is being considered because it may be more mechanically stable than the other designs when hit by a severe shock. The compromise we make is that the feed structure is not strictly TEM, so the signal may spread out (increasing the risetime) as it progresses along the feed.

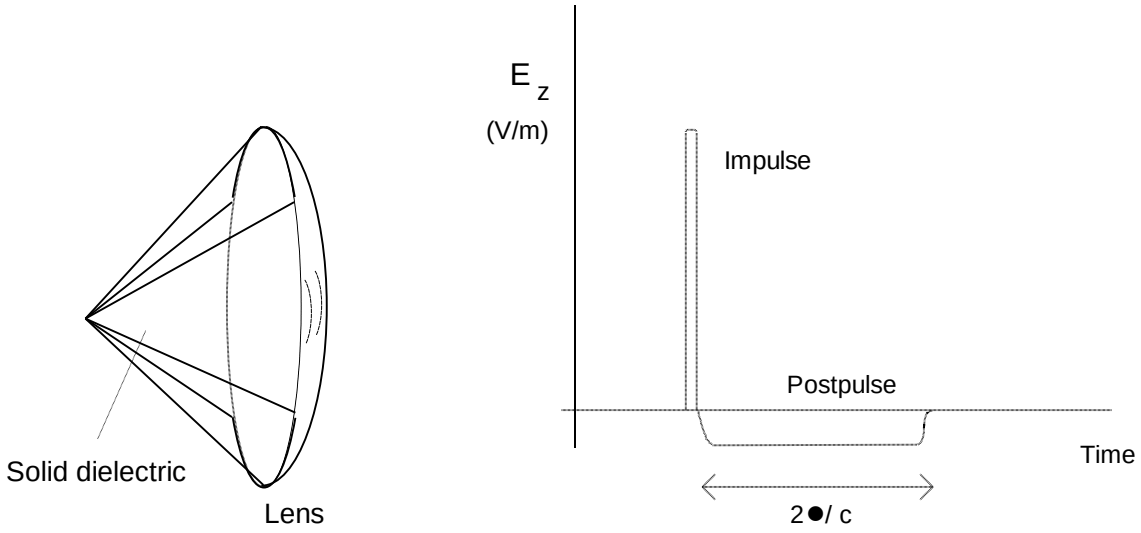

Figure 2.5. A solid dielectric lens IRA (left) and an example of its output (right).

The theory of this antenna has not yet been developed fully, however we expect it to behave similar to the regular lens IRA. The potential loss in risetime is difficult to analyze using simple techniques. However, this effect can be reduced somewhat by surrounding a portion of the apex with the dielectric material. This maintains a TEM structure part of the way out onto the antenna.

III. Time Domain Antenna Equations and Signal Processing

A. Antenna Equations

In order to understand the data we are measuring, it is important to identify the equations that describe antennas in the time domain. In particular, it is necessary to establish a relationship between the antenna's behavior in transmission and reception.

In the experiments that we carry out later, we characterize an antenna by using two identical antennas. The simplest way of doing this is shown in Figure 3.1. We describe here how to extract an antenna's characteristic function, $h(t)$ from this experimental test setup. We also show here how this characteristic function can be used to predict the antenna's response in both transmission and reception.

A second method of measuring the antenna's characteristics is to use a single antenna and measure the field reflected from a large conducting sheet. This second method is most appropriate for small antennas, because the sheet otherwise has to be too large. Later, we measure our antennas using both techniques. The signal processing is essentially the same using the two techniques, to within a minus sign. The only difference is that when using a single antenna with a reflector, one must subtract out the background noise, whereas when using two identical antennas, the background noise is less of a problem and can usually be ignored.

When describing the theory of these antennas, we express the various signals on the antenna in terms of voltage waves, much in the same spirit as S-parameters are used in microwave network theory. This does not introduce any ambiguity because almost all UWB antennas have a TEM feed, in order to maintain the risetime. Thus, voltage measurements are all made with matched loads.

$$Z_c = f_g \, 377\,\Omega$$

Figure 3.1. The relevant quantities for specifying antenna performance in the time domain for transmission (left) and reception (right).

In transmission we express the radiated field (on boresight for dominant polarization) as [2,5]

$$\begin{aligned} E^{rad}(r,t) &= \frac{1}{r} F(t) \circ V^{inc}(t) \\ &= \frac{1}{r}\left[\int_0^t F(t')\, dt' \right] \circ \frac{d V^{inc}(t)}{d t} \end{aligned} \tag{3.1}$$

Note that it is trivial to extend the above relationships to other polarizations and other angles. It is perhaps more helpful, at this point, to keep the expressions as simple as possible. When the same antenna is used in receive mode, we have [2,5]

$$V^{rec}(t) = h(t) \circ E^{inc}(t) \tag{3.2}$$

where we now see the $h(t)$ function that we first saw in Section II of this report. There is a simple relationship between the transmission function, $F(t)$, and the reception function, $h(t)$. Thus, we have [2,5]

$$\int_0^t F(t')\, dt' = \frac{1}{2\pi c f_g} h(t) \tag{3.3}$$

This is the essential relationship required to establish the antenna as a reciprocal device. Thus, we see that if one knows the $h(t)$ and feed impedance for a given antenna, then the antenna is completely characterized. It is interesting to note that the units of $h(t)$ must be *meters*/*second*, in order to maintain the correct units in the above equations.

So for our problem, we must take into account radiation from the antenna, reflection from the plate, and reception of the antenna. After possibly subtracting out a background signal, we measure

$$V_{rec}(t) = \frac{1}{2\pi c f_g r} h(t) \circ h(t) \circ \frac{d V_s(t)}{d t} \tag{3.4}$$

where r is the distance between the transmit and receive antennas, and $V_s(t)$ is the source voltage. We now need to determine $h(w)$ and $h(t)$ from the above measured voltage. To do so, we must convert to the Fourier domain. Thus, we find.

$$h(w) = \sqrt{\frac{2\pi r c f_g V_{rec}(w)}{jw \; V_s(w)}} \tag{3.5}$$

and $h(t)$ can be found with an inverse Fourier transform.

B. Phase Unwrap

In the final step of the above analysis, one must take the square root of a complex transfer function. This must be done with care, because the square root of a complex number has two values, and the correct value must be chosen at each frequency point. (Another way of saying this is one must use the correct branch cut.) A sketch of a typical phase plot is shown on the left in Figure 3.2. If one takes the square root of a function whose phase is wrapped, then one would simply divide the phase by two. This results in a function that is constrained to have a phase between $+90^o$ and -90^o. This is clearly nonphysical, since the algorithm must work for arbitrary antenna functions.

Conceptually, the simplest way of solving this problem is to subtract $N \times 360^o$ from the phase of each point, where N is an integer chosen to make the phase curve smooth. This is shown on the right in Figure 3.2. One would then take the square root by dividing the phase by two, and taking the square root of the magnitude. However, it is numerically clumsy to find the number of phase wraps for each point that will make the phase curve smooth, so we have to find another way.

A better approach is to multiply the frequency domain waveform by a suitable time delay, e^{jwt_d}. If one chooses t_d correctly, one can eliminate most of the phase wraps, leaving few or none to repair. One then needs to have a suitable way of finding t_d. There is probably some art to this. However, we propose to use a t_d equal to the time from the beginning of the waveform to its peak. Thus, before taking the square root, we convert the waveform to the time domain and note the time between the beginning of the waveform and its peak, and use this value for t_d in the phase unwrap algorithm.

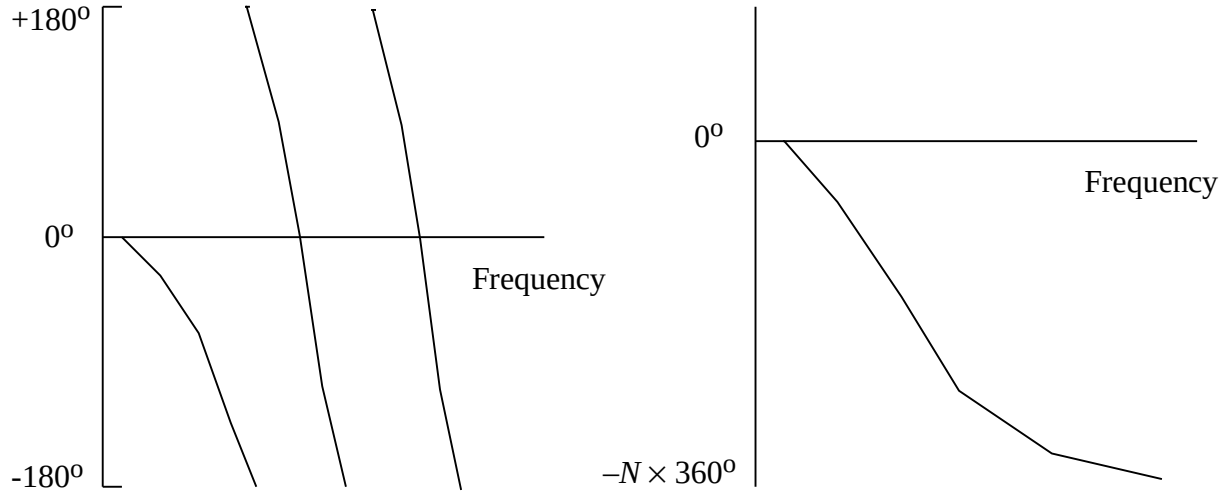

Figure 3.2. Illustration of phase unwrap before (left) and after (right).

To justify this rather simple algorithm, we note that the Fourier transform of a delta function with a time delay, $d(t - t_d)$, is just e^{-jwt_d}. Thus, to remove the phase wraps in the frequency domain, multiplying by our factor of e^{jwt_d} will exactly remove all phase variations. While our measured data are not as simple as a delta function, the algorithm seems to unwrap satisfactorily most of the signal, as we will see in our later examples.

Note that it is actually simpler to carry out the phase shift in the time domain. If one is careful about how the FFT is implemented, a translation in the time domain is exactly equivalent to a phase shift in the frequency domain. This is due to the "circular convolution" property of a discrete FFT.

After unwrapping using the phase shift, there can be a few wraps left in the data. For this second part of the phase unwrap we propose using the following simple algorithm for our phase unwrap. If the n^{th} frequency point has a phase between -90^o and -180^o, and the $(n+1)^{th}$ frequency point has a phase between 90^o and 180^o, then we decide that a phase wrap has occurred. When a phase wrap occurs, we subtract 360^o from the phase of all points after the wrap. While this algorithm was never implemented during this project, it seems reasonable to try in future work.

C. Filters

When dealing with real data there is always noise which must be filtered. We typically apply a lowpass filter to our data as required, and the filter is of the form

$$G(f) = \frac{1}{1 + (f / f_o)^{2N}} \tag{3.6}$$

where f_o is the cutoff frequency and N is some integer greater than or equal to 1. For a fifth-order filter, we use $N = 5$ in the above equation. A typical example with f_o = 20 GHz is shown in Figure 3.3.

The above filter is related to a standard Butterworth filter, in that it has an amplitude dependence that is the square of a Butterworth filter [12]. This filter has the characteristic that its inverse transform is real, since $G(f) = G^*(-f)$. However, this filter is different from standard Butterworth filters in that the phase is zero for all frequencies. Thus, the filter is unrealizable from circuit elements. This is not a strict requirement for filters when implemented on a computer, but it does render the filter noncausal. We believe that this does not produce a problem, because the filter has the intended effect on the data, as we shall see. Nevertheless, it will be of interest in future work to experiment with other forms of the above filter.

Throughout this report, the above filter will be referred to as a "modified Butterworth filter," for purposes of clarity.

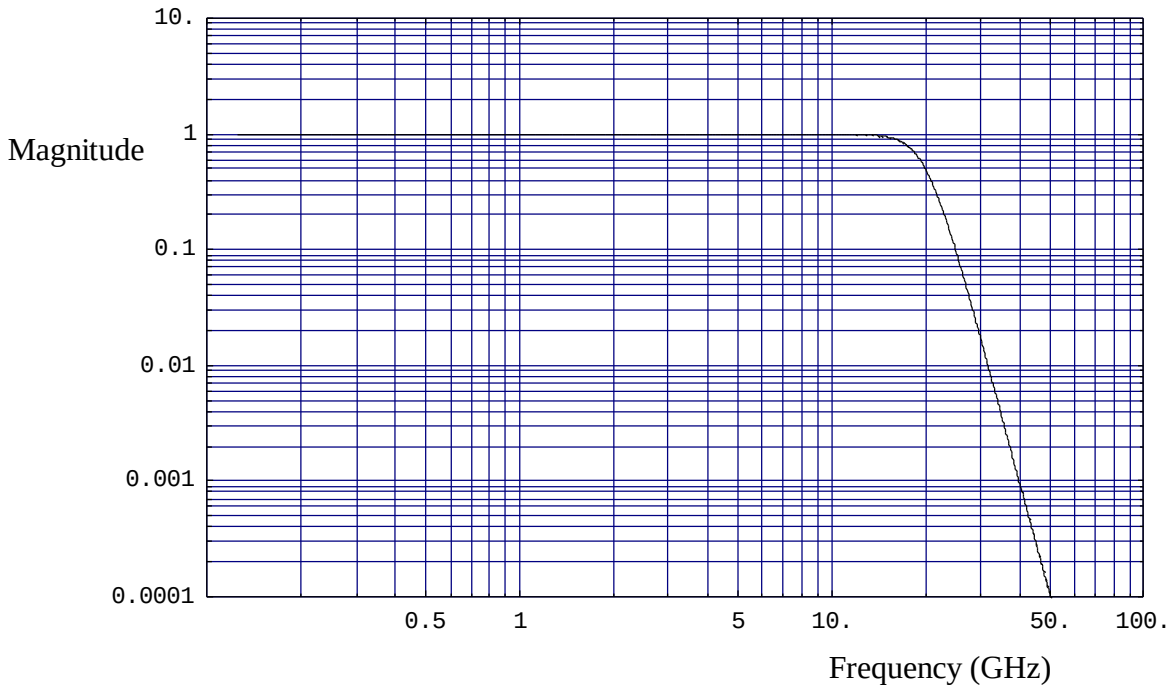

Figure 3.3. A fifth order modified Butterworth filter with f_o = 20 GHz.

IV. Reflector Size and Distance Considerations

When making measurements, it is important to be in the far field. Furthermore, when using a single antenna with a reflecting plate, the size of the plate must be large enough not to introduce error. We consider here both of these issues.

One of the difficulties here is that the term "far field" is not rigorously defined in the time domain. We propose here a simple working definition that may be adequate for our purposes. We propose that one is in the far field of an antenna when a ray from the outer edge of the antenna arrives no later 1/3 t_r after the ray arriving from the center of the antenna. Here we use t_r as either the risetime of the driving signal, or approximately the Full Width Half Max of the radiated field. The geometry is shown in Figure 4.1 for the case of a single antenna with a reflecting plate. Note that the plate must be in the far field of the antenna, since the same antenna is used for both transmission and reception. For the configuration with two identical facing antennas, one would need to separate the two antennas by $2d_1$, since both antennas are electrically large. If an electrically small B-dot or D-dot probe were used, it could be placed at a distance of d_1 in front of the antenna.

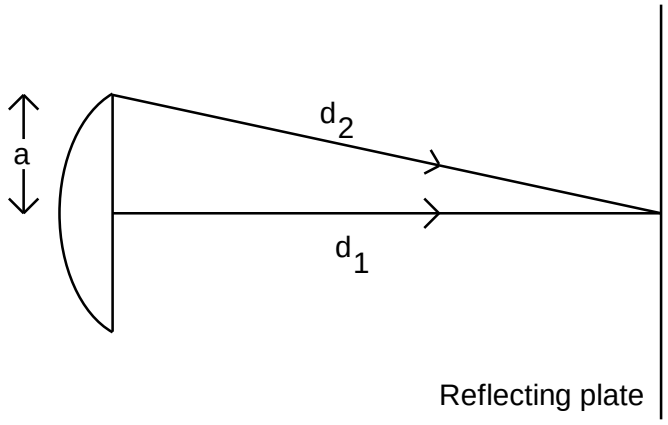

Figure 4.1. Far field calculation.

Thus, to be in the far field, the clear time between the arrival of the closest ray and the arrival of the outermost ray should satisfy

$$d_2 - d_1 \;=\; \sqrt{{d_1}^2 + a^2} - d_1 \;\le\; c\,t_r \,/\, 3 \tag{4.1}$$

In the usual case, $a << d_1$, so

$$d_1(1+a^2/2d_1^2) - d_1 \le ct_r/3$$
$$d_1 \ge \frac{3a^2}{2ct_r} \tag{4.2}$$

If, for example, $a = 23$ cm, and $t_r = 100$ ps, then d_1 must be larger than 2.6 m. We must emphasize that this is an approximation, and that there is as yet no universal agreement on the definition of far field in the time domain.

We must also calculate the size of the plate necessary to prevent scattering from the plate edges from contaminating the data. Thus, we propose that it is necessary to maintain a clear time t_c in order to prevent edge effects from entering into the time window of the measurement. The configuration is shown in Figure 4.2. From this diagram, we require

$$ct_c > 2(d_3 - d_1) = 2\sqrt{d_1^2 + \Delta a^2} - 2d_1 \tag{4.3}$$

Solving for Δa, we find

$$\Delta a > d_1\sqrt{\left(\frac{ct_c}{2d_1}+1\right)^2 - 1} \tag{4.4}$$

If, for example, $a = 23$ cm, $t_c = 2$ ns and $d_1 = 2.6$ m, then $\Delta a = 1.28$ m. The overall radius of the reflecting plate is then the sum of $a + \Delta a$, or 1.54 m. This will provide a clean signal out to 2 ns.

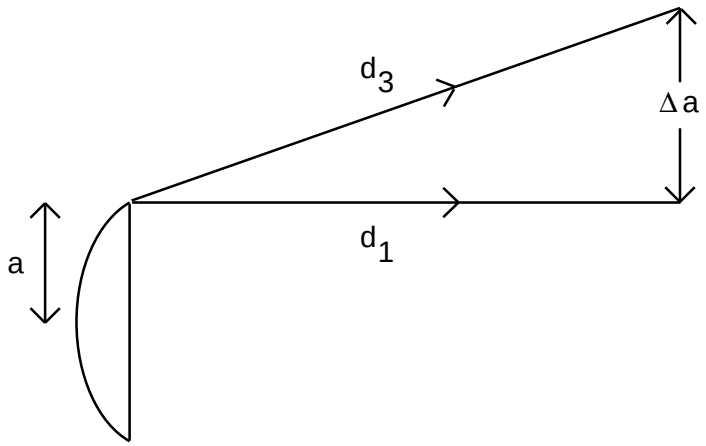

Figure 4.2. Calculation for determining the size of the reflecting plate.

V. Effect of the Balun and the Second Pair of Arms

All of our theory for the radiated fields has been calculated for a certain voltage across a single pair of arms. In practice, for the reflector IRA, there will be a balun and two pairs of arms. It is important to understand how the voltage on the feed line relates to the voltage across a single pair of arms. The balun we use here was first described by C. E. Baum, in [6], and is shown in Figure 5.1.

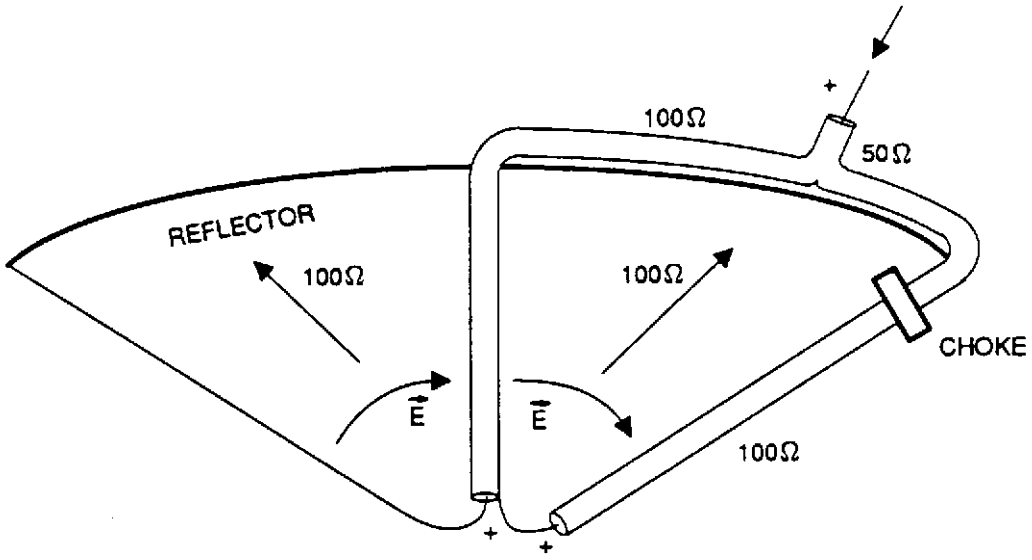

Figure 5.1. A 50 Ω to 200 Ω balun for a reflector IRA.

To analyze the balun, we use the configuration sketched in Figure 5.2. It consists of two 100 Ω line sections that are connected in parallel at the input end (giving 50 Ohms) and in series at the output end, giving 200 Ohms. The net effect is that a 1 V signal on the feed line is transformed into a 2 V signal across each pair of orthogonal feed arms. Note that the 200 Ω length of line is included for clarity in the diagram, but it is not needed, nor is it used in the actual balun.

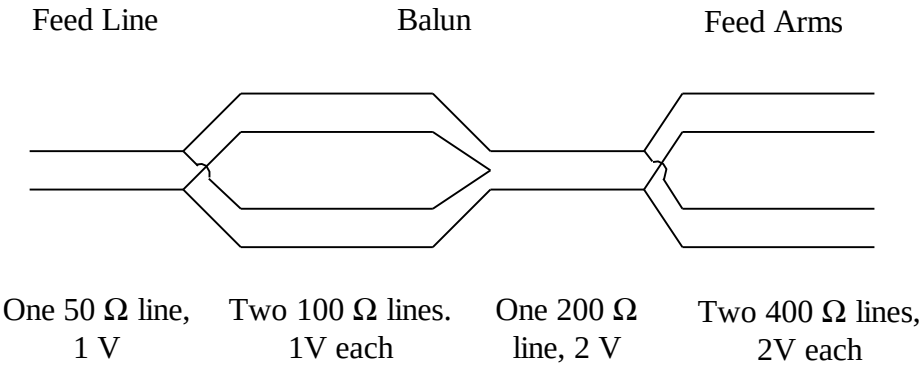

Figure 5.2. The voltages and feed impedances of the geometry at various points along the feed.

The consequences of this model are as follows. All of the equations developed thus far to describe the radiated field are expressed in terms of the feed voltage across a single pair of feed arms. There is a factor of 2 difference between the feed line voltage and the feed arm voltage. Furthermore, if we have two pairs of arms at 45^o instead of a single pair of arms, the radiated field must be multiplied by an additional factor of $\sqrt{2}$. Thus, for our configuration, if the source voltage in our equations is the voltage on the feed line, then the radiated field must be multiplied by a factor of $2\sqrt{2}$. In reception, one must divide by the same factor of $2\sqrt{2}$.

VI. Predictions of Fields and Voltages

We provide here predictions for the radiated field and the received voltage for a reflector IRA in front of a large reflecting plate. It is assumed that we have a single reflector IRA with F/D = 0.25 or 0.667. The reflector has a radius of 23 cm, and the reflecting plate is 2.5 m in front of the antenna. The smooth-step source has a peak voltage of 200 mV, with a risetime of 100 ps.

The driving voltage is assumed to be an integrated Gaussian of the form [7]

$$\frac{dv(t)}{dt} = \frac{V}{t_d} e^{-p(t/t_d)^2}, \qquad t_{FWHM} = 0.940\, t_d \tag{6.1}$$

$$v(t) = \int_{-\infty}^{t} \frac{dv(t')}{dt'}\, dt', \qquad t_{10-90} = 1.023\, t_d \tag{6.2}$$

where t_{FWHM} is the Full Width Half Max of dv/dt, and $t_{10\text{-}90}$ is the 10-90% risetime of $v(t)$. These waveforms are plotted in Figure 6.1. Recall the definition of the derivative risetime of a waveform is

$$t_d = \frac{\max\,(v(t))}{\max\left(dv(t)\,/\,dt\right)} \tag{6.3}$$

Thus, the derivative risetime is inversely proportional to the maximum derivative of the driving voltage. This is a useful property, since the peak of the radiated field is proportional to the peak of the derivative of the voltage. Note also that for the integrated Gaussian waveform, the derivative risetime t_d is within two percent of the 10-90% risetime, $t_{10\text{-}90}$. In our case V = 200 mV, and t_d = 100 ps. A plot of the driving voltage with the correct scaling is shown in Figure 6.2.

Using eqns. (6.1) and (2.1-2.2), we find the radiated field shown in Figure 6.3 This is the field found after the field radiates from the antenna, reflects off the plate, and returns to the same antenna for reception (after traveling 2 × 2.5 meters). Note that the 200 mV driving voltage refers to the voltage on the 50-Ohm feed line, so we have included an extra factor of $2\sqrt{2}$ as described in the previous section. The received voltages are shown in Figure 6.4. This is the voltage as measured on the 50-ohm output cable.

Finally, we note that it is possible to correct for feed blockage using a factor calculated in [13, Figure 5.5]. For a 400 Ω feed (single pair of arms), one would multiply the entire waveform by a factor of 0.92 for a single pass through the antenna, or by a factor of $(0.92)^2$ = 0.85 for two passes through the antenna. This correction is based on the fast portion of the waveform, so it is actually an approximation to apply this to both the fast and slow portions of the waveform. Our calculations in this section have not used this correction factor, but calculations in Sections VIII and IX of this note will use this factor.

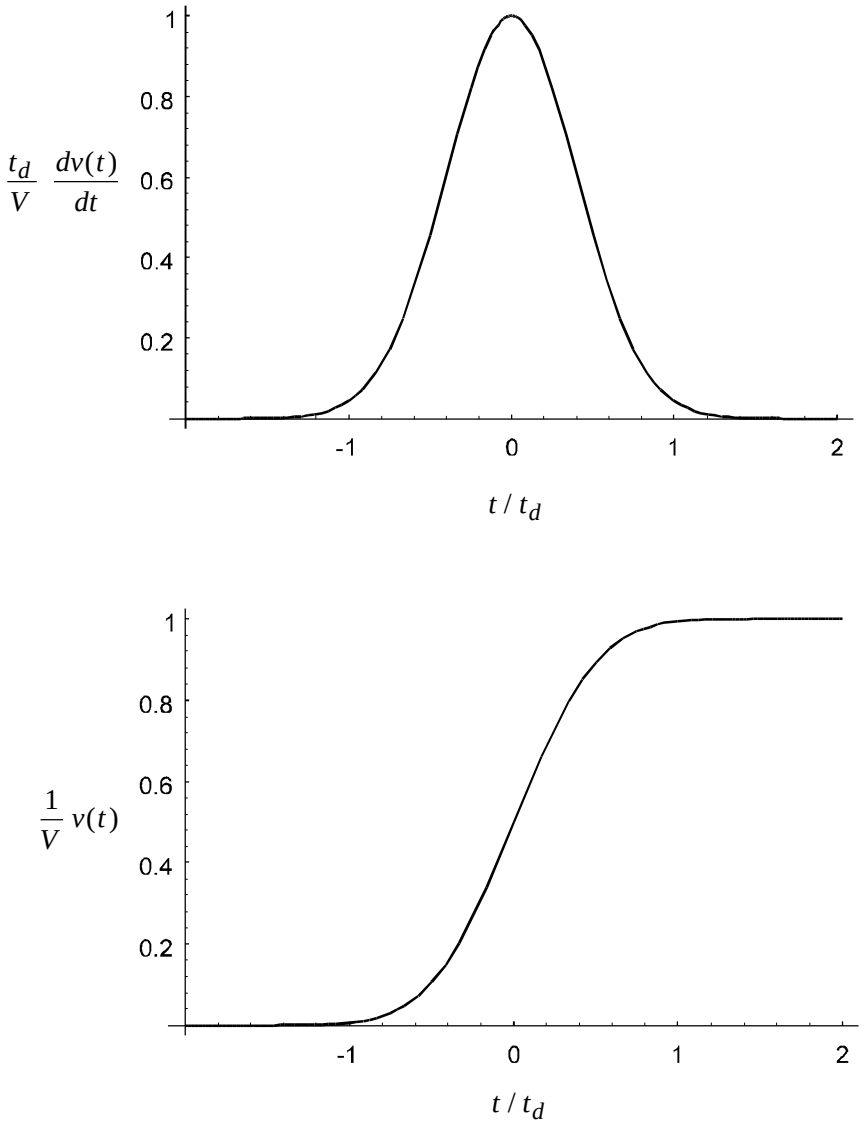

Figure 6.1. Derivative of driving voltage (top), and its integral (bottom).

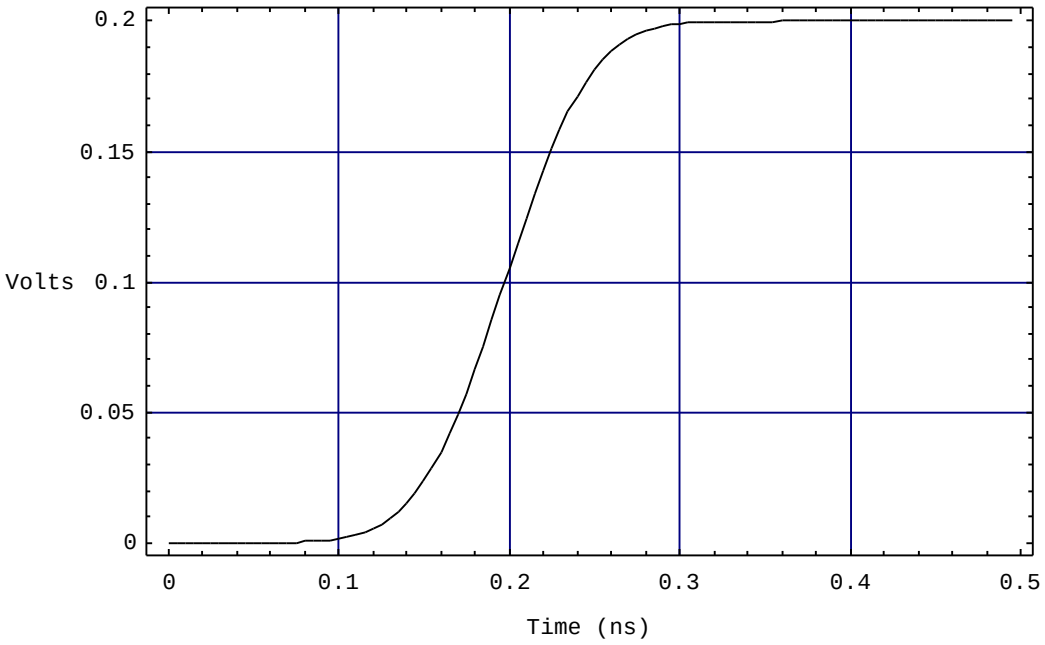

Figure 6.2. Driving voltage scaled to the parameters of the current problem.

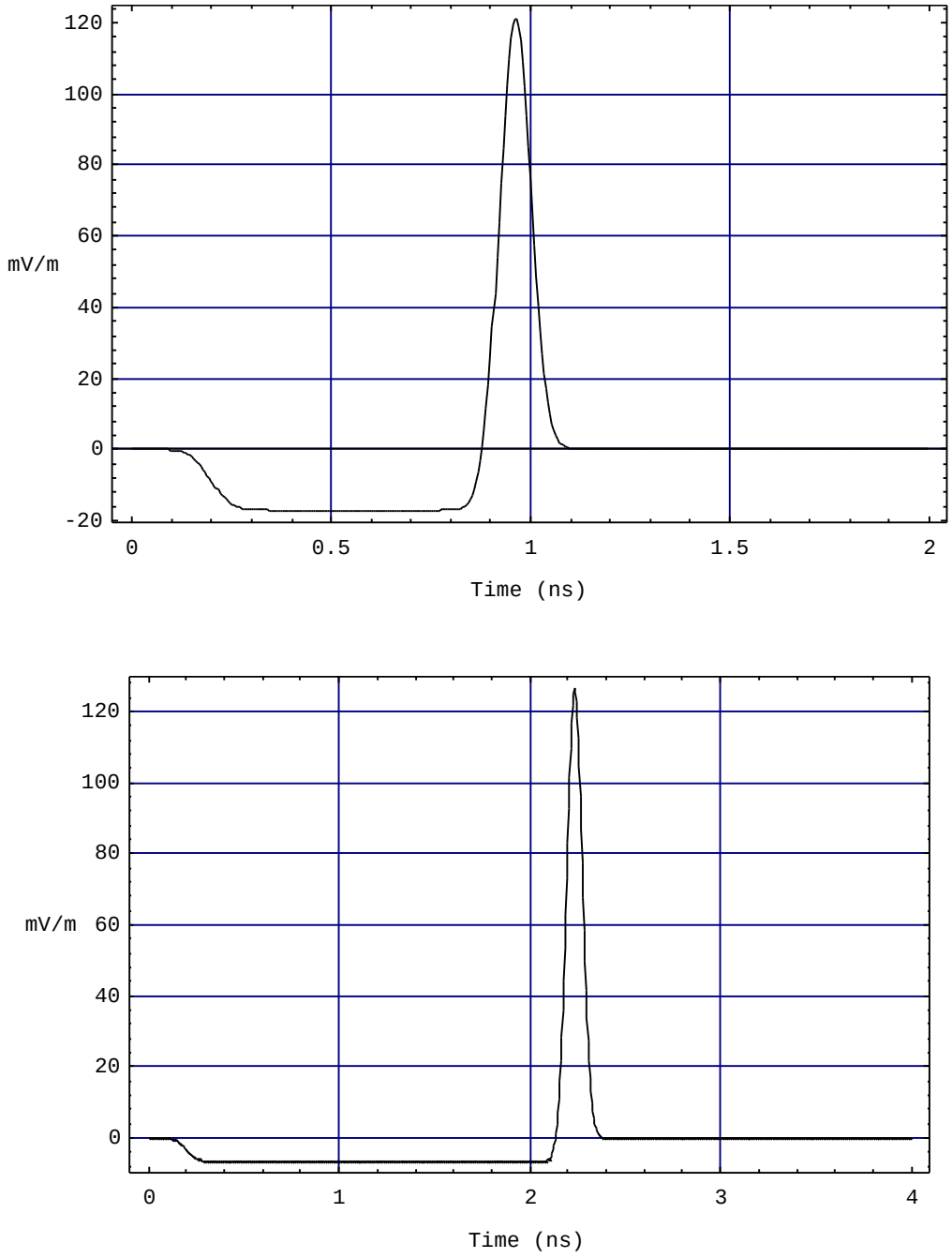

Figure 6.3. The radiated field at the location where it is received by the antenna under test, for $F/D = 0.25$ (top) and $F/D = 0.667$ (bottom).

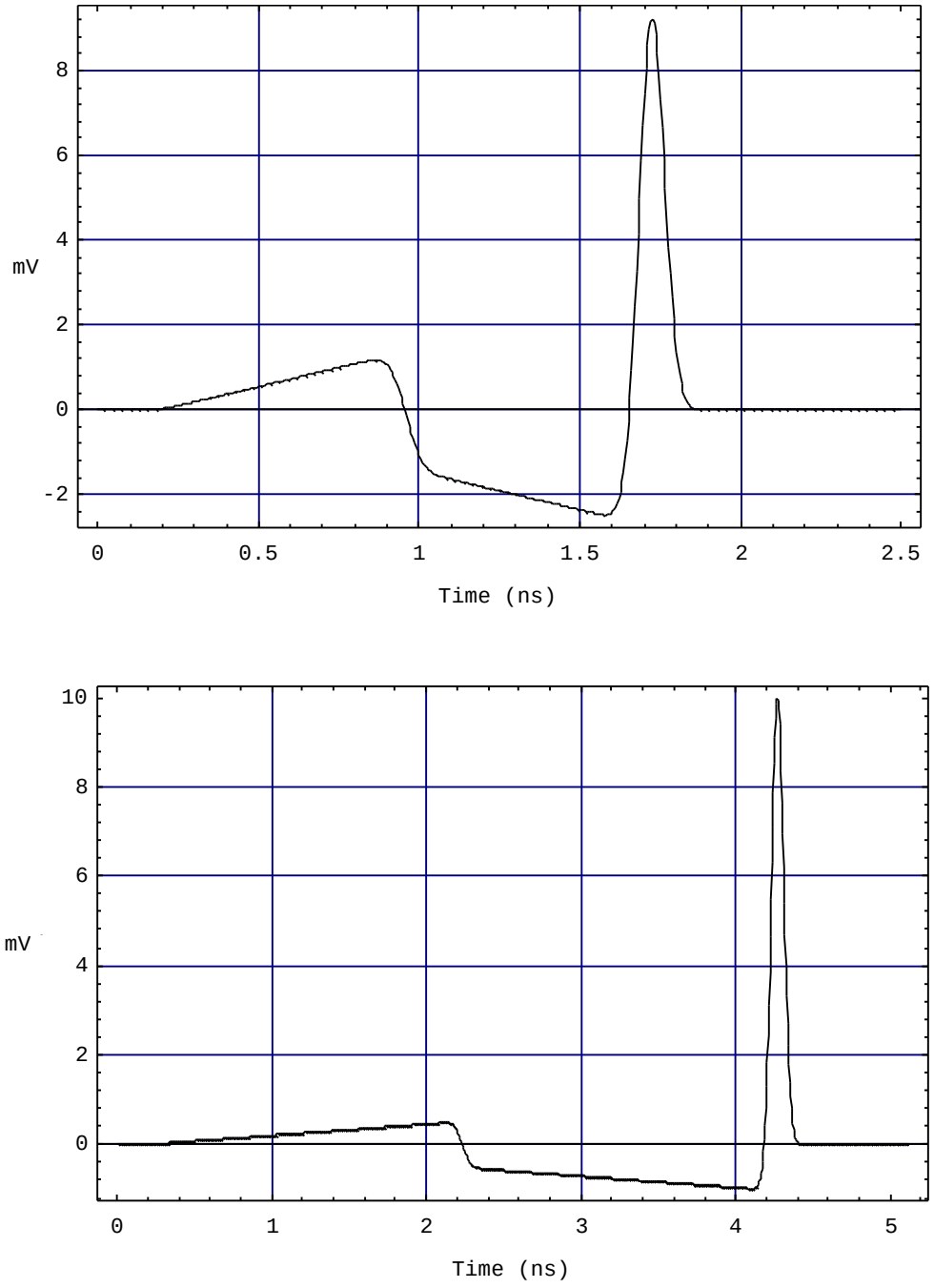

Figure 6.4. The received voltage for $F/D = 0.25$ (top) and $F/D = 0.667$ (bottom).

VII. Antenna and Balun Construction and Preliminary Measurements

We consider here the construction of the reflector IRA and the integrated balun. We provide measurements of the balun's performance, and we demonstrate compensation for the cables in the balun. Finally, we measure a TDR at the antenna input, which leads after some processing to a frequency domain return loss. We begin with the antenna and balun construction.

A. Antenna and Balun Construction

Two 46 cm diameter reflector IRAs were built with F/D of 0.25. The four feed arms were constructed using the "coplanar plate geometry," meaning that they were constructed from two flat sheets of metal oriented perpendicular to the aperture plane to minimize feed blockage. With $F/D = 0.25$ and $Z_c = 400\ \Omega$, the arms were perfectly vertical with a 16.3^o angular width. More precisely, using the angles described in Figure 2.3, $b = 90^o$, $b_1 = 98.1^o$, and $b_1 = 81.8^o$. The feed arms were shorted to the reflector. A sketch of the antenna as built appears is Figure 7.1.

A balun was integrated into the antenna as shown in Figure 5.1. The balun assembly consists of a 12.1 cm length of 0.085 inch diameter, 50-ohm semi-rigid input cable, joined to two parallel 37-cm lengths of 0.141 inch diameter semi-rigid 100-ohm cable. The equal-length 100-ohm cables were connected in series at the feed point. The cable dielectric is PTFE with a dielectric constant of 2.01. The 50 ohm to 100 ohm junction in the balun was encased in a molded epoxy housing for physical support. This had no effect on the electrical properties of the unit, which are excellent, with less than 5% reflection coefficient for 40 picosecond resolution TDR.

A trade-off between risetime and voltage hold-off capability is made at the feed point. A spacing of approximately 6 mm is maintained at the feed point to allow voltages of several kilovolts without dielectric breakdown. The loss in risetime from the spacing appears to be acceptable, since the measured response of the antenna is well below the 100 ps requirement. Some fine tuning of the feed geometry was required to optimize the system risetime. A set screw and sliding mechanism allowed adjustment of the feed point location over a distance of ±1 cm. The antenna is mounted on a 1.2 meter tripod, which allows accurate adjustment of azimuth and elevation. This is essential due to the narrow beam width.

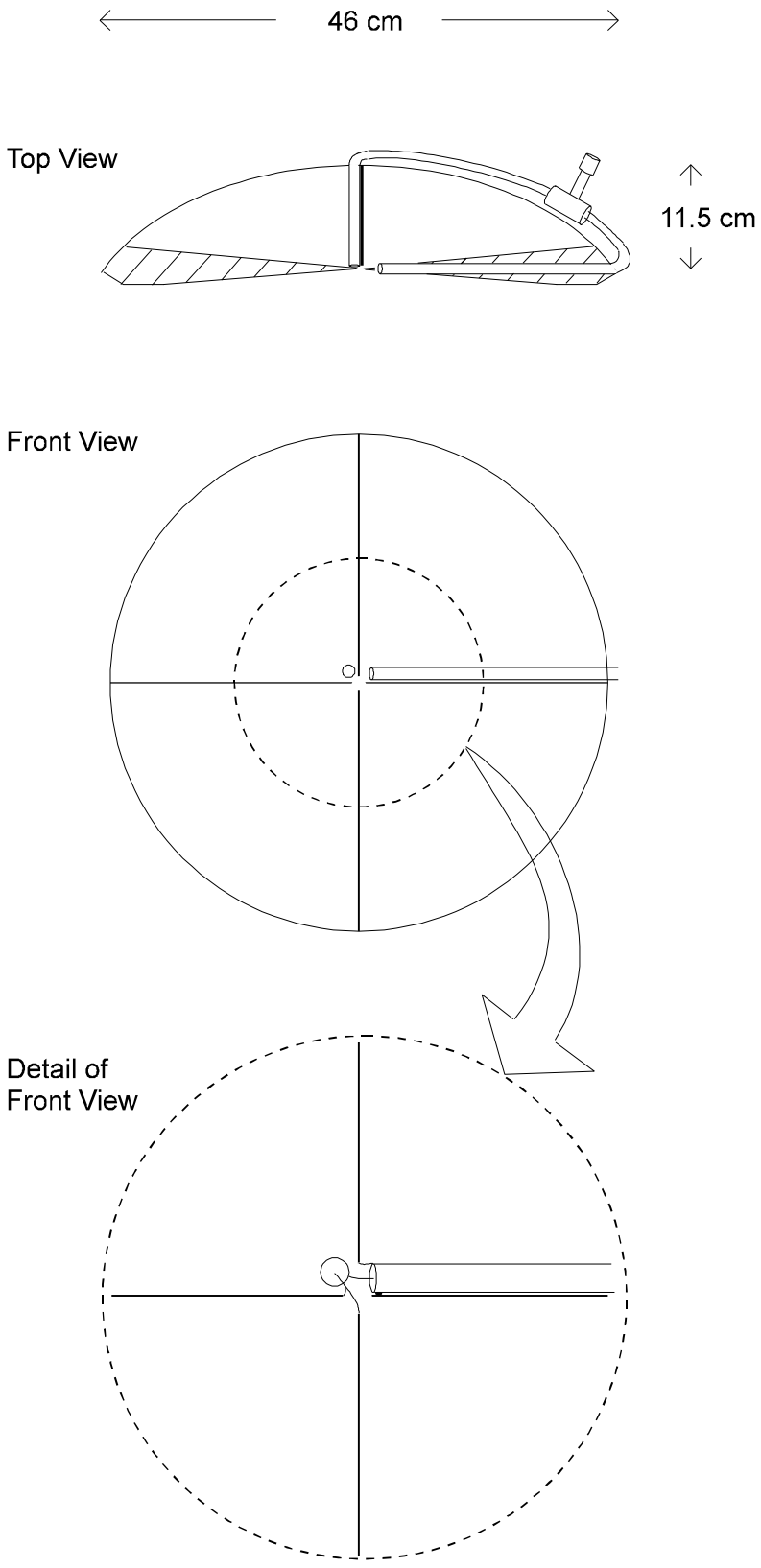

Figure 7.1. The reflector IRA as built.

B. Balun Measurements

We measured first the effect that the balun has on the overall system performance. This was accomplished by shorting out the far end of the balun at the apex of the antenna, and comparing the reflected pulse to the incident pulse.

The test setup is shown in Figure 7.2. The step pulse was generated by the HP model 1106B tunnel diode pulser, which provides a transition between two dc levels. The transition amplitude is approximately 220 mV and the transition time less than 20 picoseconds (10% to 90%). The tunnel diode pulser is mated directly to the 28 ps risetime sampling head, HP model 1817A, using APC-7 connectors. The combined response of the tunnel diode pulser and sampling head was confirmed to be less than 40 picoseconds by terminating the pulse directly at the head in a HP model 909A precision termination with APC-7 connectors. For antenna testing, the termination was removed and a metrology grade adapter from APC-7 to SMA was connected to a 61-cm length of Gore-Tex port cable. This high quality cable uses foamed Teflon dielectric and is mode free to 33 GHz. The cable is connected to the 50 ohm input of the IRA antenna.

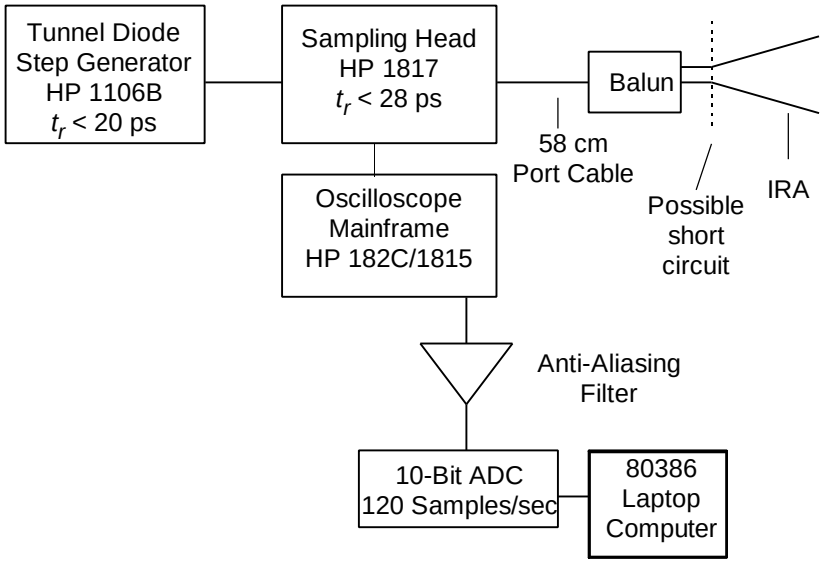

Figure 7.2. The experimental configuration used to test the frequency response of the balun and also used to measure the TDR of the IRA radiating into free space.

The sampling head was controlled by an HP 1815 sampling plug-in in a model 182C mainframe. The sampling plug-in allowed variable sweep speed and vertical gain. The analog output of the sampling plug-in was passed through a low pass filter with RC = 4 msec to a 10 bit ADC which was sampled at the rate of 120 samples per second. The data acquisition was controlled by an 80386 based laptop computer and data was streamed directly to the disk. This system is highly oversampled.

We were careful to perform accurate calibration of time and amplitude. Time calibration was accomplished with a calibration fixture consisting of a short length of 100 ohm cable mismatched to the 50 ohm system. The fixture was connected in place of the antenna and excited by the tunnel diode pulser to produce a stairstep waveform with a characteristic time of 1.47 ns. The amplitude calibration was accomplished by reference to a low-impedance DC source read-out on a 4 digit digital volt meter for accurate calibration of the tunnel diode amplitude. We then used a precision microwave variable attenuator to adjust the tunnel diode pulser voltage for calibration of the more sensitive ranges and to characterize linearity. With these procedures, time and amplitude calibrations are believed to be accurate to ±3% over the full range of experimental parameters.

The measurements and data processing proceeded as follows. We first measured the output of the source directly, as shown in Figure 7.3. Next, we measured the reflection from the balun with the apex short circuited. The reflection from the short is shown in Figure 7.4.

The derivatives of the source and the reflection from the short are shown in Figures 7.5 and 7.6, respectively. Note that we have filtered both sets of data with a fifth-order modified Butterworth low-pass filter with a cutoff frequency of 20 GHz. Note also that we show only the portion of the derivative waveforms near the impulse, for clarity. Ideally, one would expect these two waveforms to be approximately equal, however, there is some loss and dispersion through the 48-cm balun cables and the 61-cm port cable. The t_{FWHM} of the pulse goes from 38.5 ps to 51.7 ps after being reflected. Furthermore, the area of this derivative pulse goes from 0.225 to 0.197 V. Finally, the peak magnitude at the input goes from 5.61 V/ns to 3.34 V/ns. Clearly, it will be important to account for cable losses to obtain good agreement between theory and measurements.

Finally, we characterized the losses in the frequency domain. We did so by calculating the frequency domain ratio of the derivative of the reflection from the short (Figure 7.6) to the derivative of the source voltage (Figure 7.5). Note that we retained the data over a 10 ps time window when taking the Fourier transform. The result is shown in Figure 7.7. As expected, the losses are relatively low at low frequencies, increasing somewhat at higher frequencies. This plot is probably valid only up to 10 GHz or so, but we include data up to 20 GHz to allow the reader to decide.

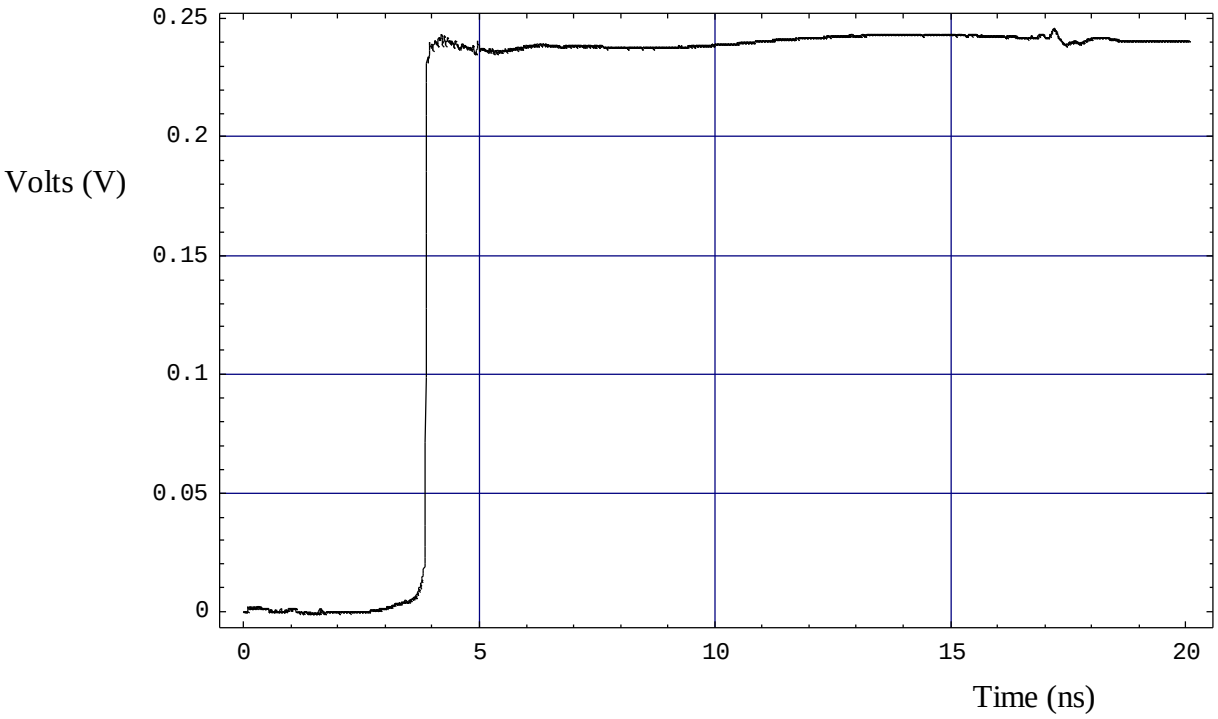

Figure 7.3. The source waveform.

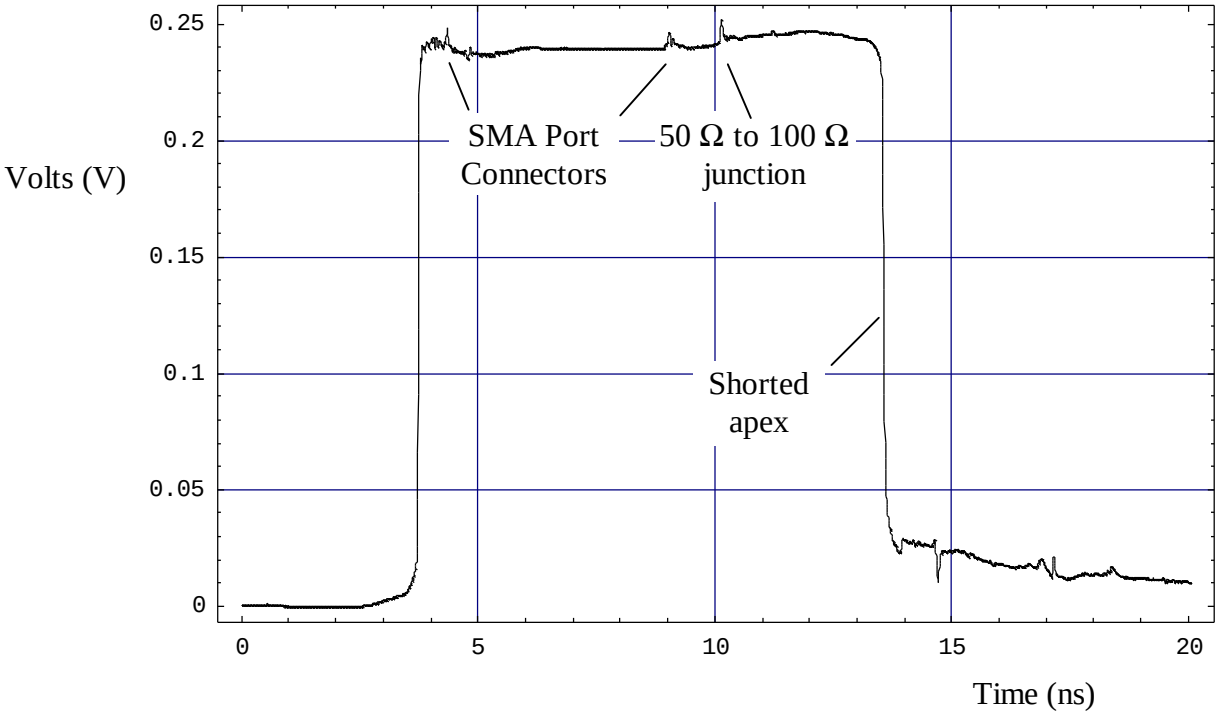

Figure 7.4. The reflection from the short.

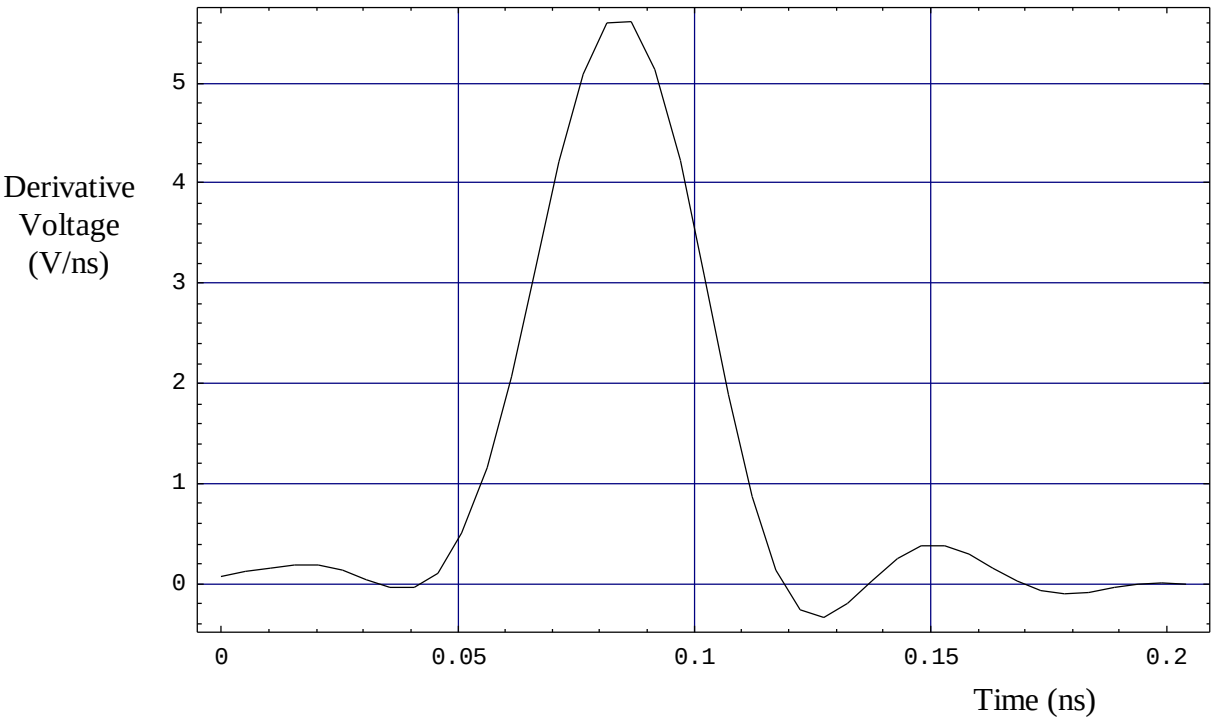

Figure 7.5. Derivative of the source waveform. Note that t_{FWHM} = 38.5 ps, area = 0.225 V, and the peak = 5.61 V/ns.

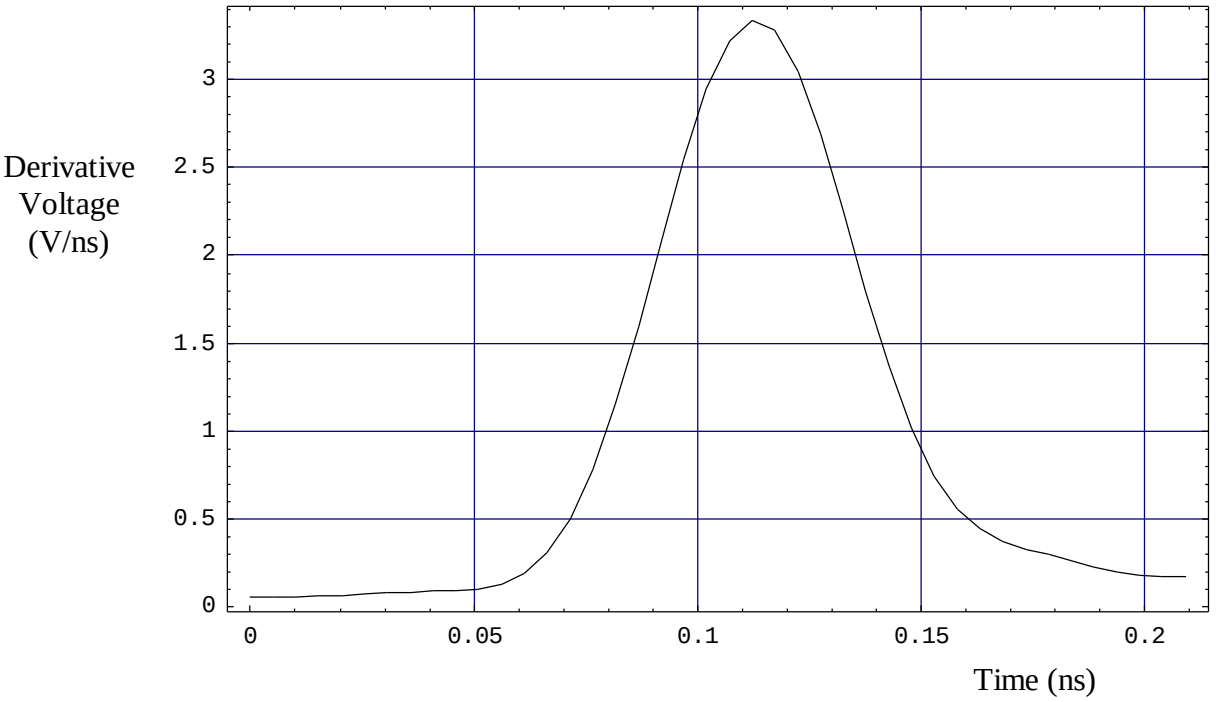

Figure 7.6. Derivative of the reflection from the shorted apex. Note that t_{FWHM} = 51.7 ps, area = 0.197 V, and the peak = 3.34 V/ns.

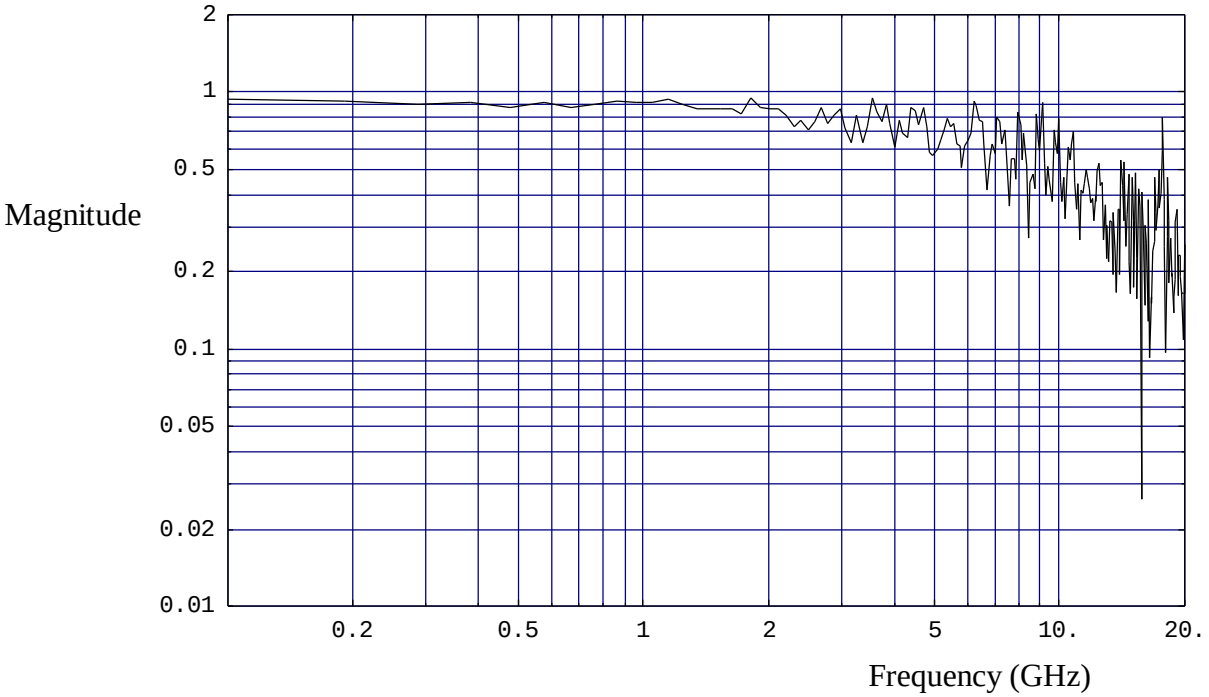

Figure 7.7. Ratio of the derivative of the reflection from the short to the derivative of the source. The data is probably valid only up to 10 GHz.

C. Antenna TDR and Return Loss

Next, using the same test setup as in Figure 7.2, we removed the short from the antenna apex to measure the TDR of the antenna radiating into free space. The input voltage is shown in Figure 7.8, and the reflection from the antenna is shown in Figure 7.9. Derivatives of these two waveforms are shown in Figures 7.10 and 7.11. Note that these have been filtered with a fifth-order modified Butterworth filter with a cutoff frequency of 20 GHz. As expected, we find the reflected pulse to be lacking in high-frequency content, because it has been radiated. The t_{FWHM} of the pulse goes from 39.2 ps to 338 ps after being reflected. Furthermore, the area of this derivative pulse goes from 0.222 V to 0.213 V after being reflected. Finally, the peak magnitude at the input goes from 5.40 V/ns to 0.451 V/ns. It is interesting to note that the peak and the t_{FWHM} have each degraded by about a factor of ten, but the area has remained approximately constant.

Finally we calculate the frequency domain return loss of the IRA. This is calculated by taking the frequency domain ratio of the derivative of the reflected pulse (Figure 7.11) to the derivative of the input voltage waveform (Figure 7.10). Note that we retained a 10 ps time window when taking the Fourier transform. The result is shown in Figure 7.12. Although we have displayed data as high as 20 GHz, the data is probably only valid up to about 10 GHz. We find that over a large part of the mid-band, roughly 1-10 GHz, this ratio is below 0.2. Thus, there is less than 4% (0.2^2) power reflection over a decade of bandwidth. This is excellent bandwidth performance for a high-gain antenna.

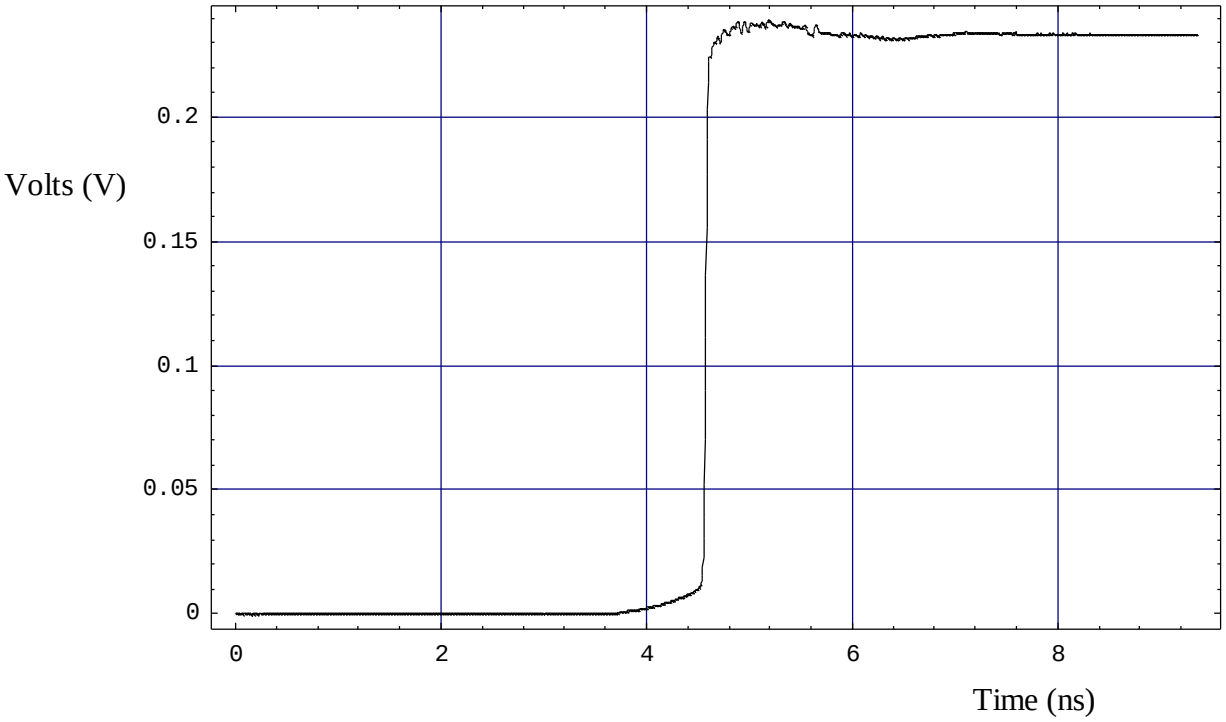

Figure 7.8. The source waveform.

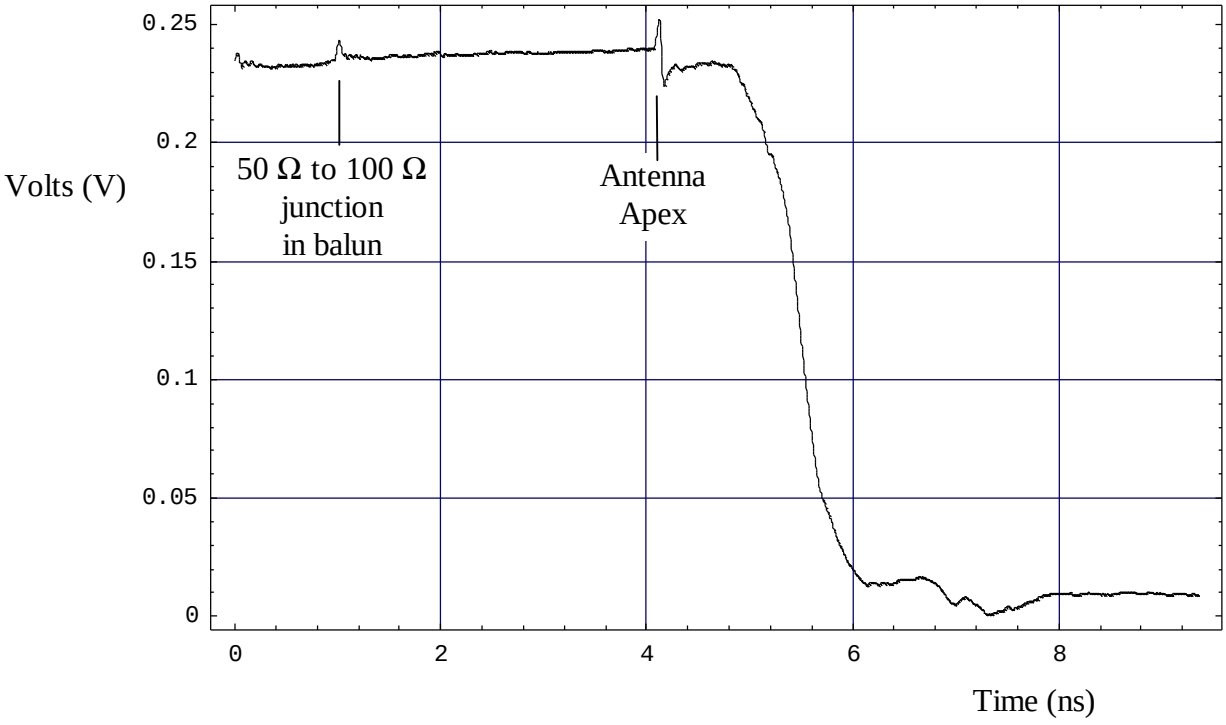

Figure 7.9. The reflection from the antenna.

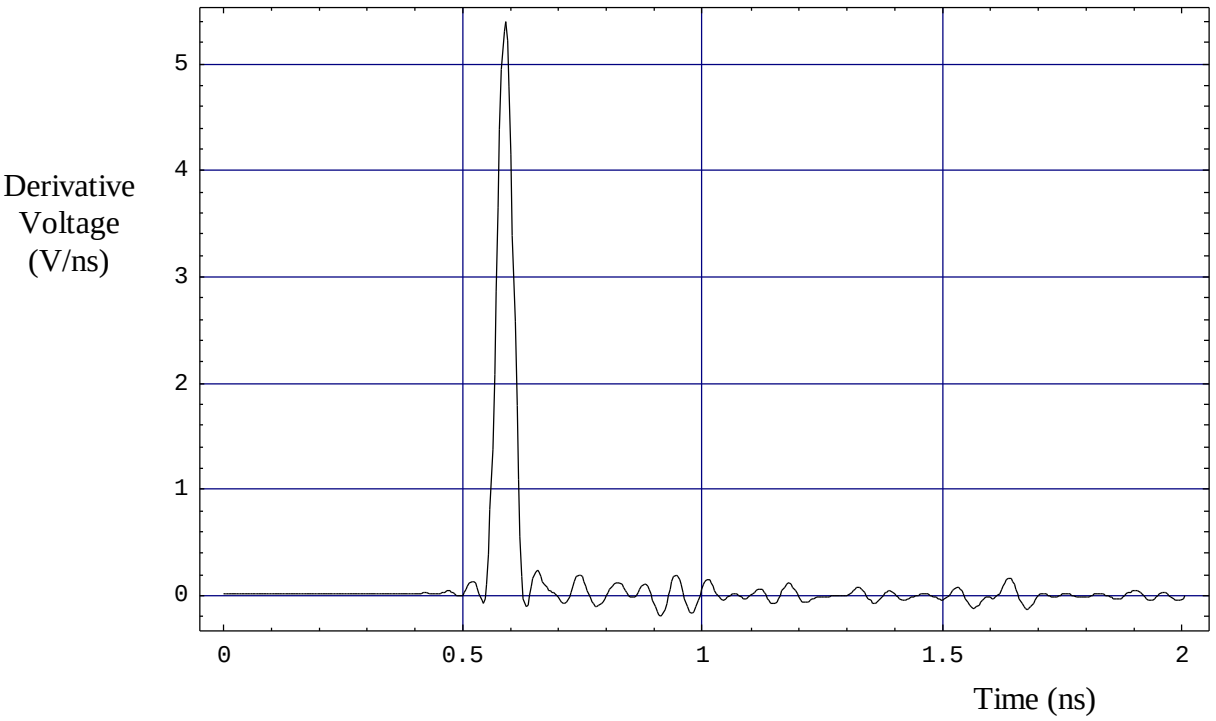

Figure 7.10. Derivative of the input voltage. Note that t_{FWHM} = 39.2 ps, area = 0.222 V, and the peak = 5.40 V/ns.

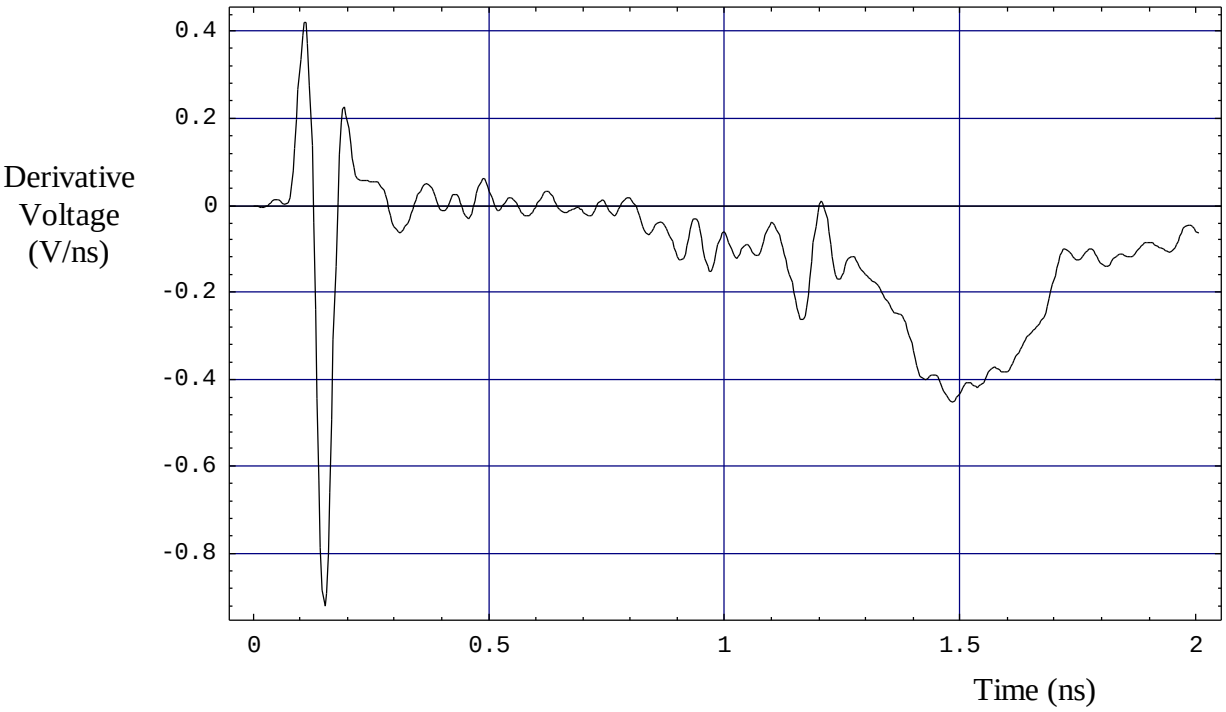

Figure 7.11. Derivative of the reflection from the antenna. Note that t_{FWHM} = 338 ps, area = 0.213 V, and the peak = 0.451 V/ns.

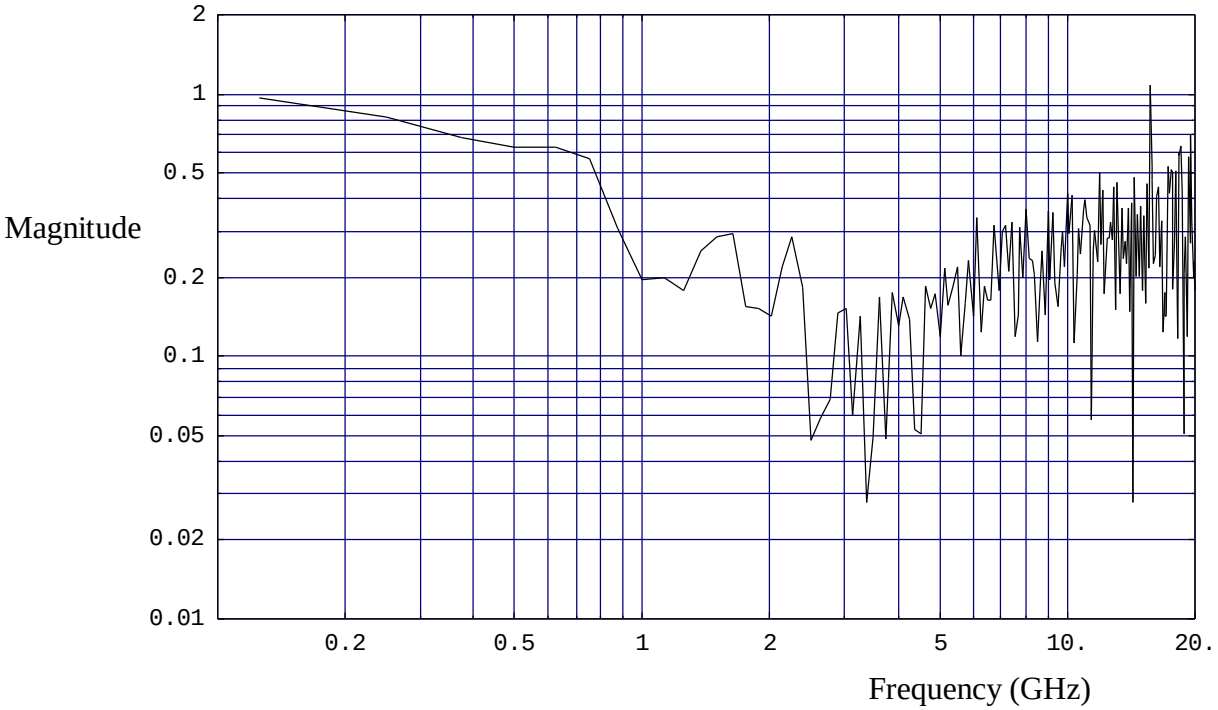

Figure 7.12. Return loss of the IRA, calculated as the frequency domain ratio of the derivative of the reflection from the antenna to the derivative of the input source voltage.

VIII. Indoor Antenna Measurement with a Large Reflector Plate

We measured the antenna's radiation characteristics using two methods. We describe here the indoor measurements, which used a single antenna and a large reflector plate. The second method, using two identical antennas, is described in Section IX. The test setup is shown in Figure 8.1. By measuring the return from the reflector, after the signal has passed through the antenna twice, we extract the one-way antenna characteristic function, $h(t)$, using the data analysis of Section III.

The IRA antenna was set on a tripod 1.2 meters above the floor in the laboratory environment and beamed down a long hallway to a 1.2 m x 2.4 m reflector plate which could be moved to control the antenna-reflector distance. Reflections from objects in the laboratory were clearly visible in the waveform, but were subtracted out by taking background data with no reflector present. It was seen that by subtracting the two waveforms virtually all the reflections disappeared except the desired signal from the reflector plate.

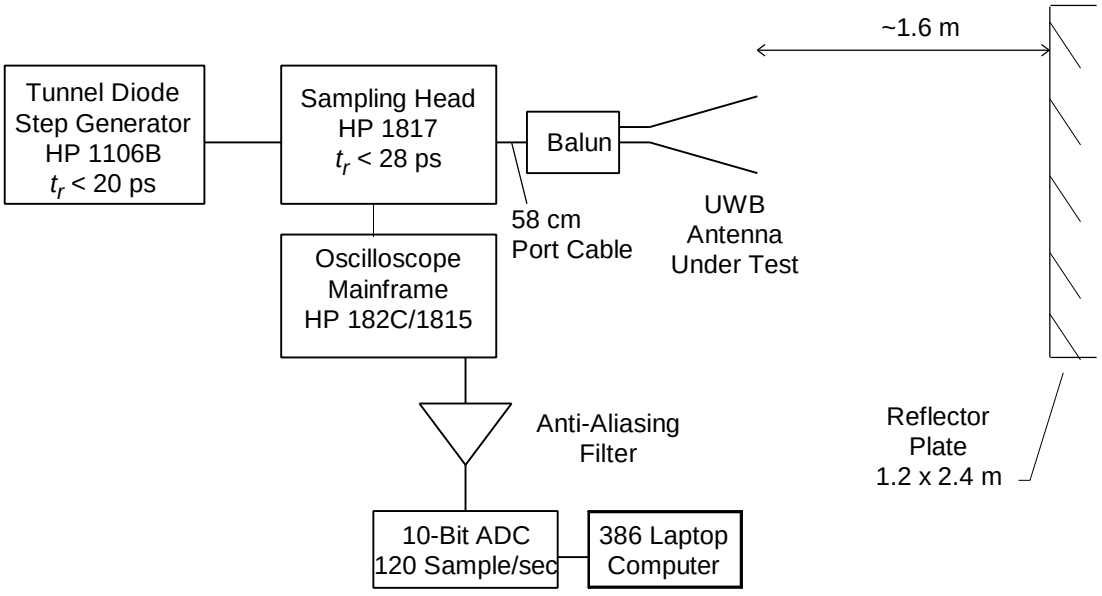

Figure 8.1. The experimental configuration used to measure the IRA's radiated field, using a single antenna with a large reflecting plate.

We began by measuring the background waveform (without the reflector plate), and then we measured the received voltage with the reflector plate in place, as shown in Figures 8.2 and 8.3. This data is highly oversampled, with a time step of 0.8 ps. In order to subtract the background from the received voltage, it was necessary to shift the data in time so their time scales would line up correctly. There are two bumps in the data sets near 3 ns and 4.2 ns, which we can use to align the data. From the bump at 4.2 ns, we find the shift to be 38 time steps, or 30.4 ps. After performing the shift, and subtracting the background, the result is shown in Figure 8.4. Note that the two bumps have essentially disappeared.

The data was then reduced by averaging every three points, and then the data was truncated at either end to give the data set in Figure 8.5. The data is now sampled at once every 2.4 ps with 2048 total points. Even after averaging, the data was still noisy, so we converted the data to the frequency domain and applied a 20th-order modified Butterworth filter whose cutoff frequency is 20 GHz. The frequency response of the filter is shown in Figure 8.6, and the resulting time domain waveform is shown in Figure 8.7. This is our final result for the measured received voltage. A close-up of the impulse is shown in Figure 8.8, where one can see the t_{FWHM} is about 70 ps for the pulse.

We now use theoretical models developed in Sections II and VI of this report to predict what the received voltage waveform should be. As we have shown in the previous section, there is some degradation in the signal as it passes (twice) through the balun and the 58-cm port cable. For this reason we use for our source the voltage reflected from the shorted apex. The voltage reflected from the short is shown in Figure 8.9, and its derivative is shown in Figure 8.10. A close-up of this waveform near its peak is shown in Figure 8.11. It is noisy, but it can be filtered using the twentieth-order 20 GHz modified Butterworth filter used earlier. The result after filtering is shown in Figure 8.12. It has a t_{FWHM} of 47 ps, and a peak dV/dt of 3.4 V/ns. Although the waveshape is not exactly Gaussian, we can approximate it as such to estimate the received voltage for our model. To do so, we use the relationships in equation (6.1) and (6.2) that $t_{FWHM} = 0.940\ t_d$, and $\max(dv/dt) = V_{max}/t_d$. Thus, we find the maximum voltage of the integrated Gaussian is 170 mV for a 50 ps t_d.

Using the V_{max} and t_d of the voltage reflected from the short, we calculate in Figure 8.7 an expected theoretical received voltage corrected for aperture blockage, as discussed in Section VI. This should be compared to the experimental received waveform of Figure 8.7. The magnitude of the prepulse is about 75% of the predicted value, while the peak magnitude of the impulse is substantially lower than the expected value. We believe the primary reason for this is that the reflector is not in the far field. To verify this, we go back to our equation for determining the location of the far field, equation (4.2). For a 70 ps pulse and a 23 cm radius, we estimate a distance of 3.8 meters is required, instead of the 1.6 meters which we used here. The field radiated from a focused aperture generally remains constant out to the beginning of the far field, and then decays as $1/r$. If we are still within the near-field region where the field is constant, our far-field theory tends to predict too high a value.

Finally, we extract $h(t)$ from the measured data using equation (3.5). Before taking the complex square root, a linear phase shift is introduced to remove most of the phase wraps. The result of this phase shift is shown in Figure 8.14. We can see that we have removed all the phase wraps at mid-band. Phase wraps at high frequencies are probably unavoidable, however, they are not important because the magnitude is very small there. There remains a single phase wrap at the low frequencies, but that probably does not introduce much error into the result.

The resulting antenna step response is shown in Figure 8.15. The function that is plotted is $h(t)/f_g^{1/2}$. Recall that equation (2.2) predicts that this should be a negative polarity step function, followed by a delta function with positive polarity. The resemblance to this is quite reasonable.

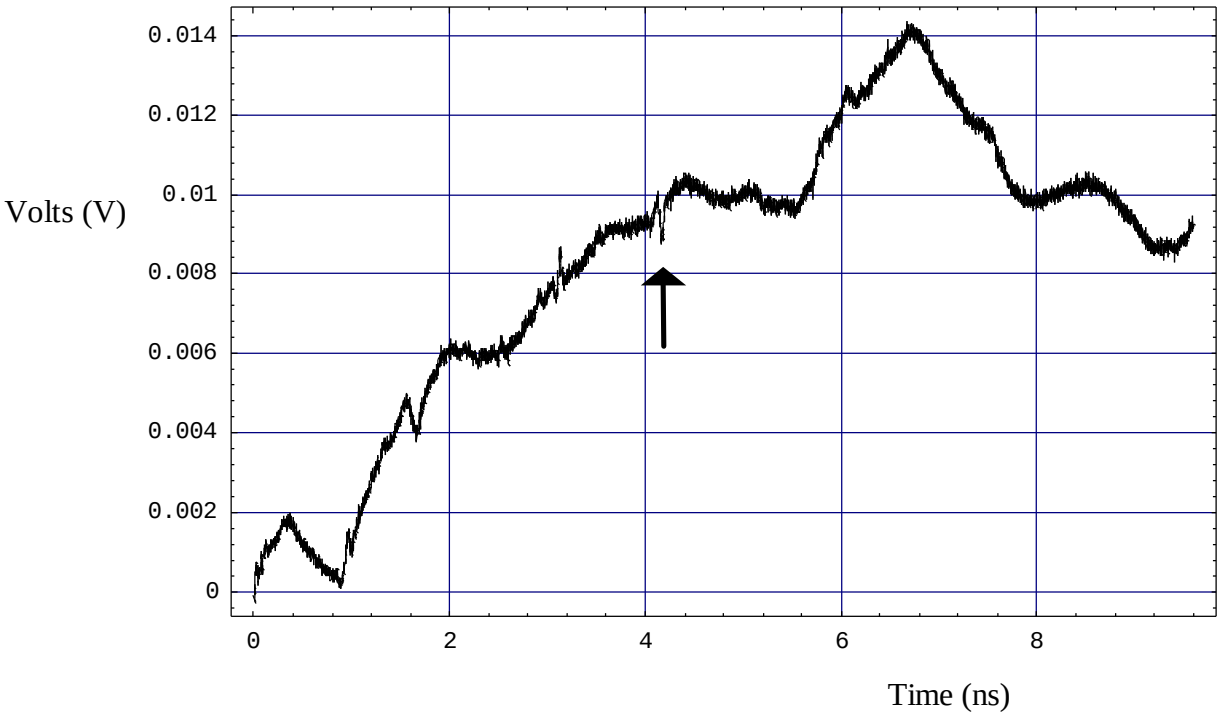

Figure 8.2. The background (no reflector plate).

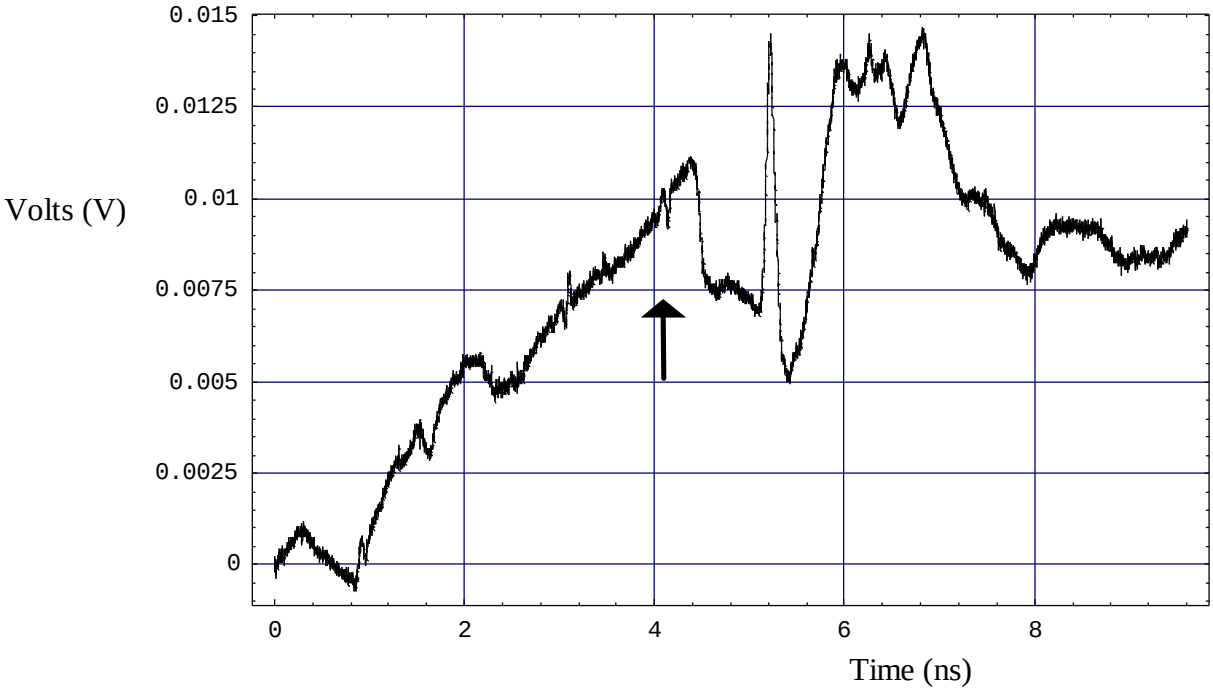

Figure 8.3. The raw received voltage (with the reflector plate in place), in the presence of a background.

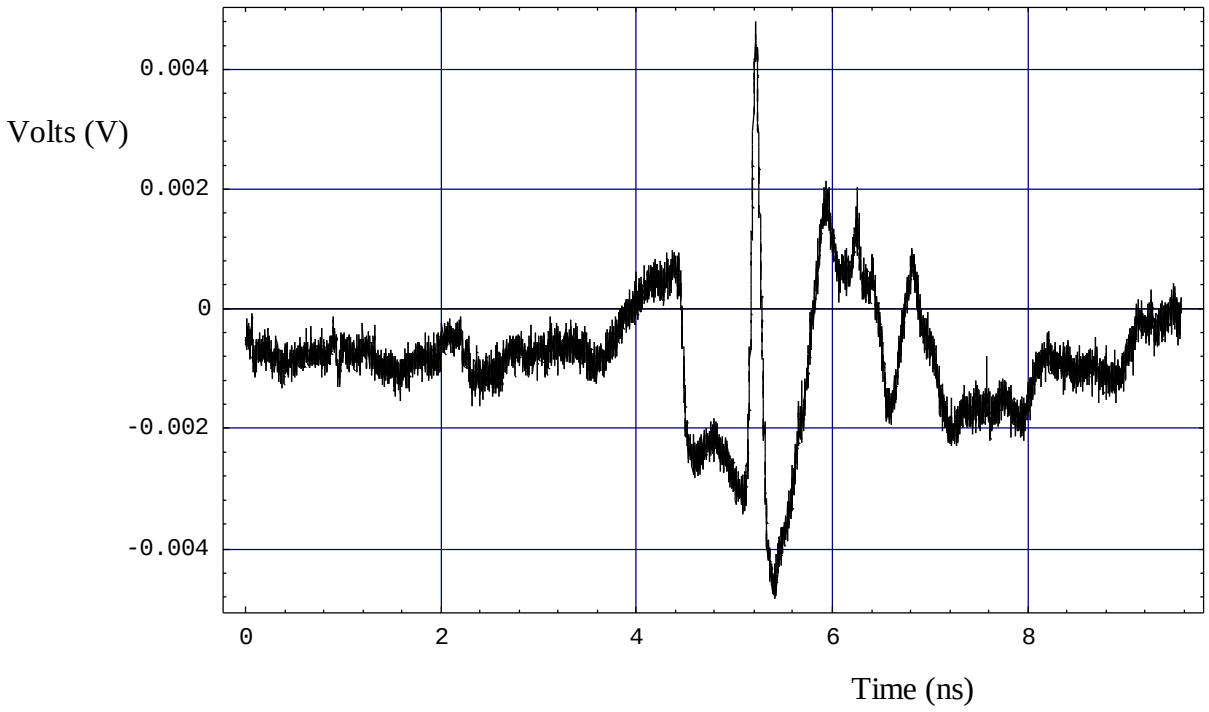

Figure 8.4. The received voltage after subtracting out the background. Note that the bump near 4.2 ns has been removed.

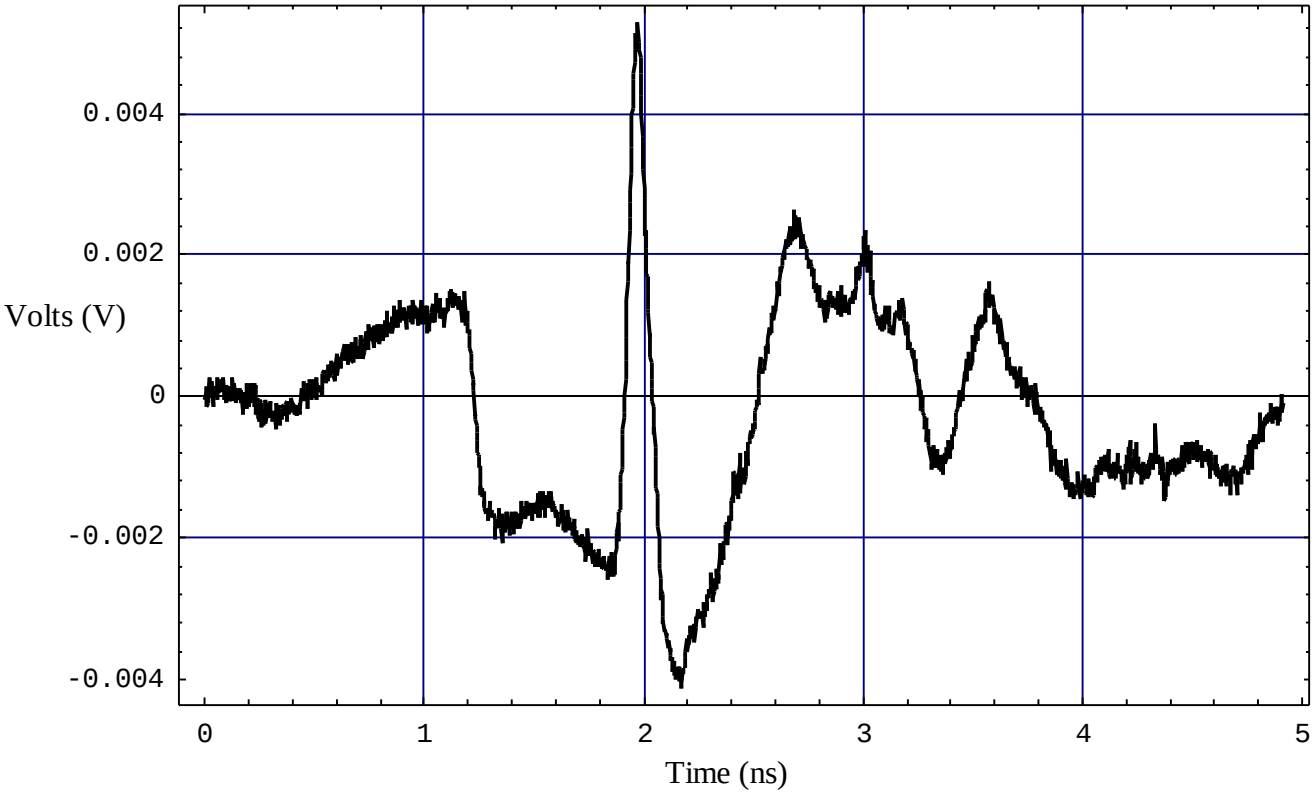

Figure 8.5. The received voltage after a 3:1 data averaging and truncation at early and late times.

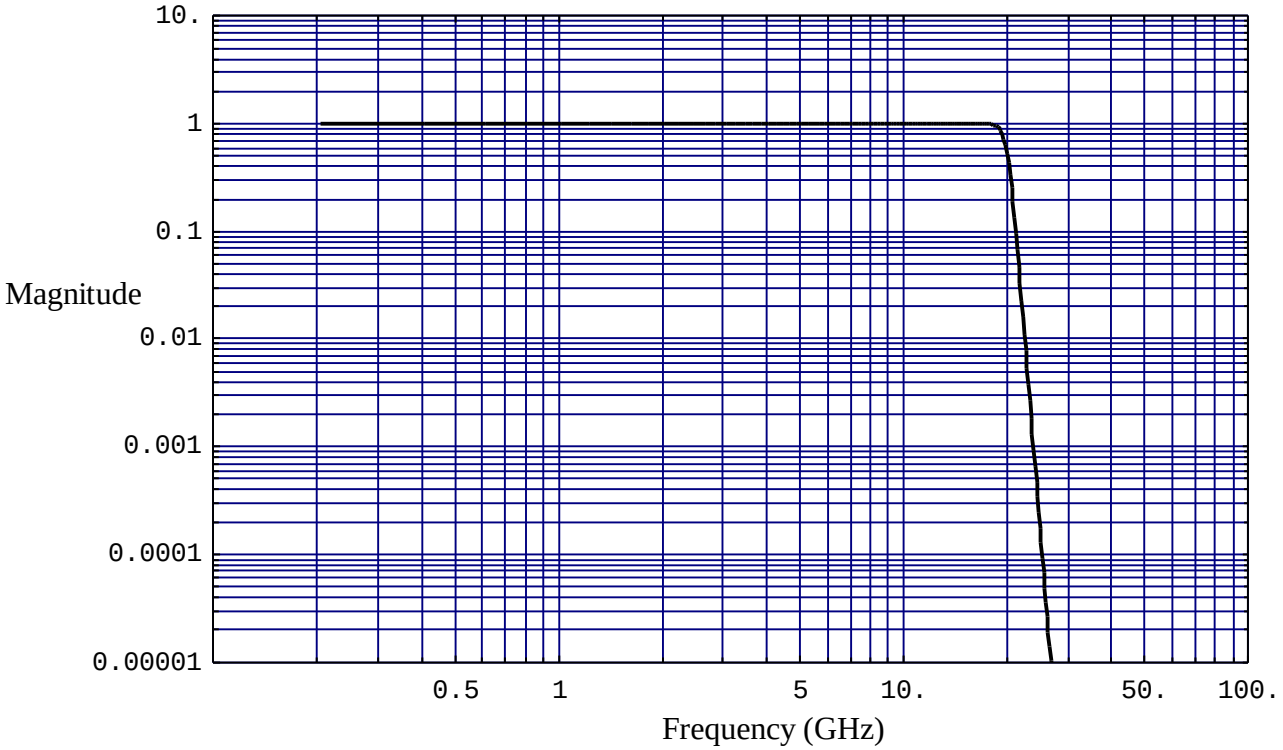

Figure 8.6. The 20th–order modified Butterworth filter used on the data

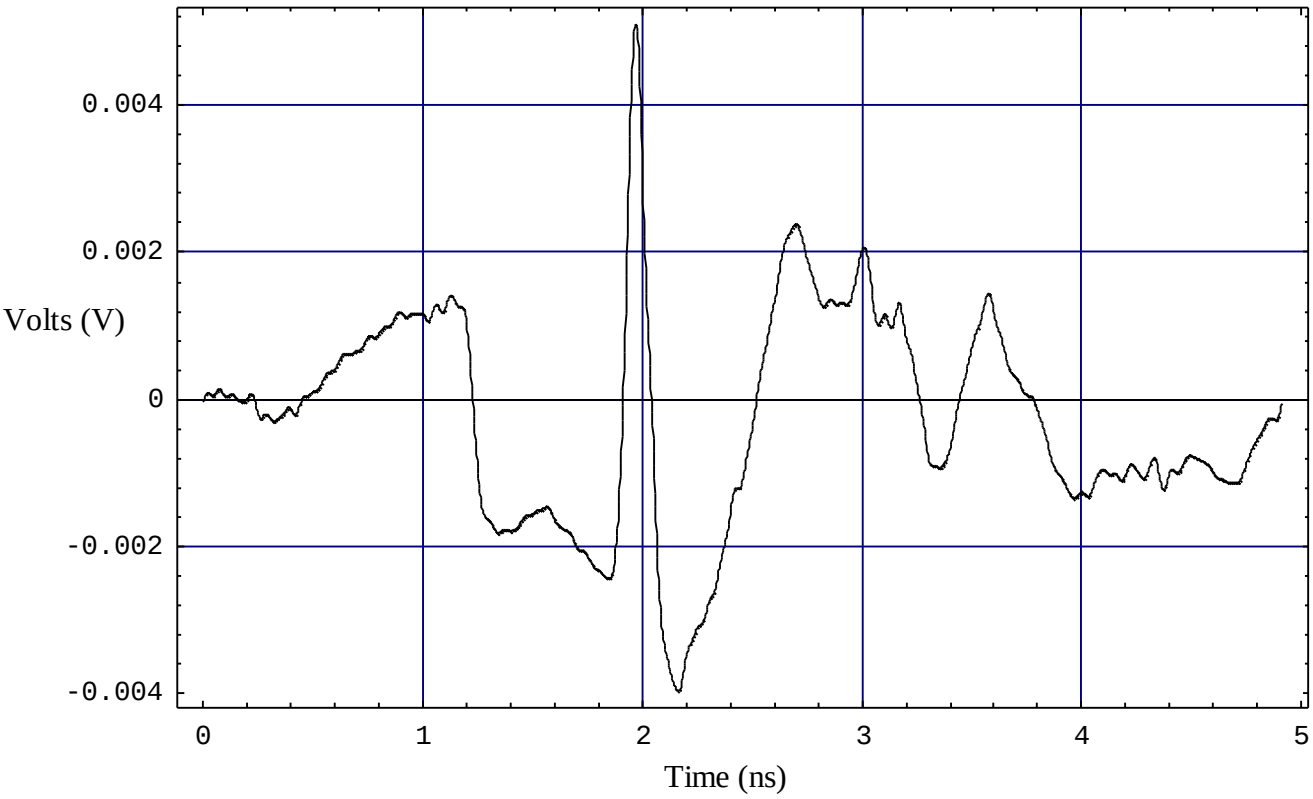

Figure 8.7. The received voltage after filtering.

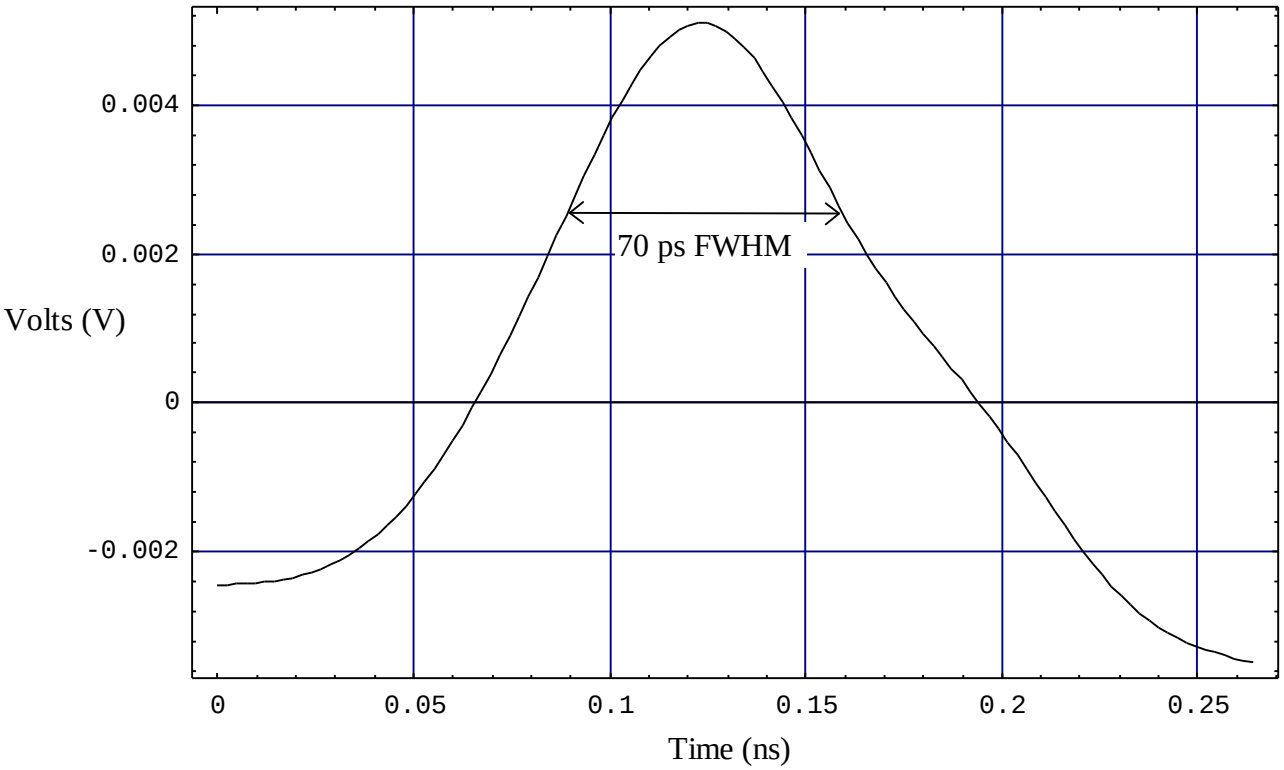

Figure 8.8. A close-up of the impulse portion of Figure 8.7.

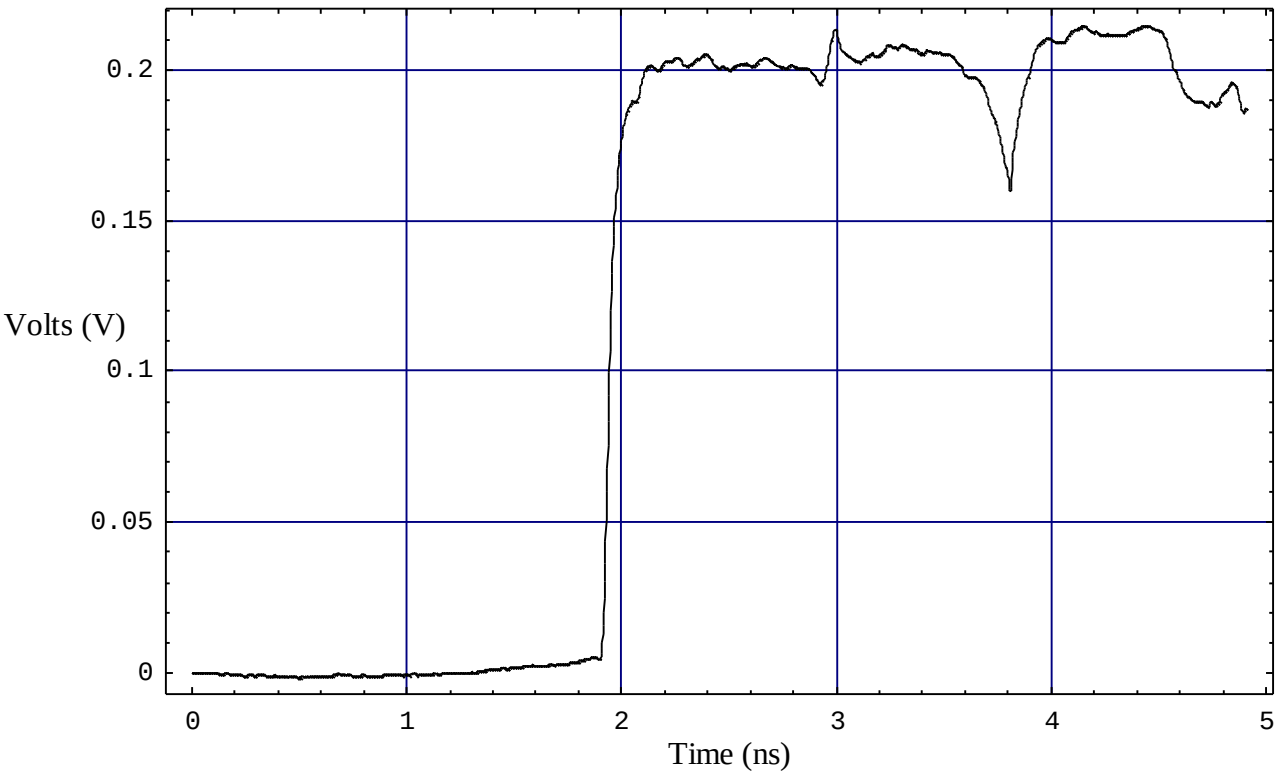

Figure 8.9. The voltage reflected from the shorted apex.

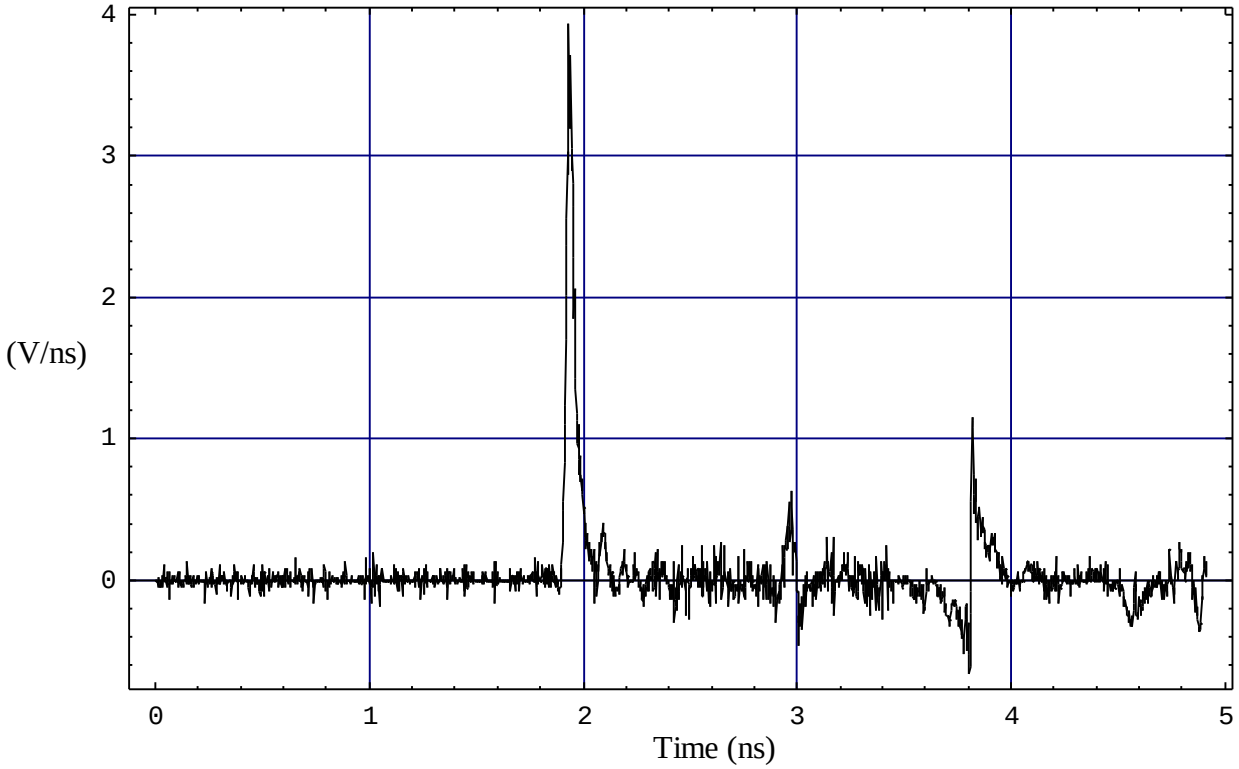

Figure 8.10. The derivative of the voltage reflected from the short.

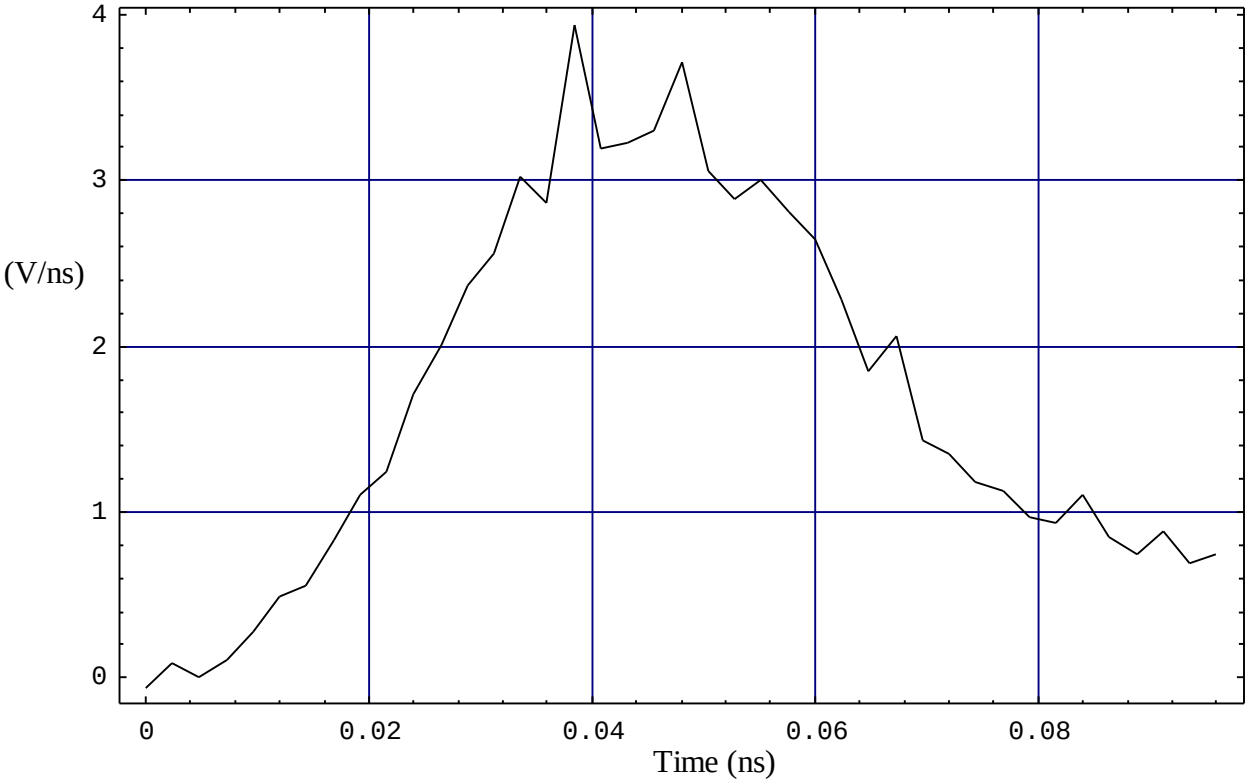

Figure 8.11. A close-up of the derivative of the voltage reflected from the short.

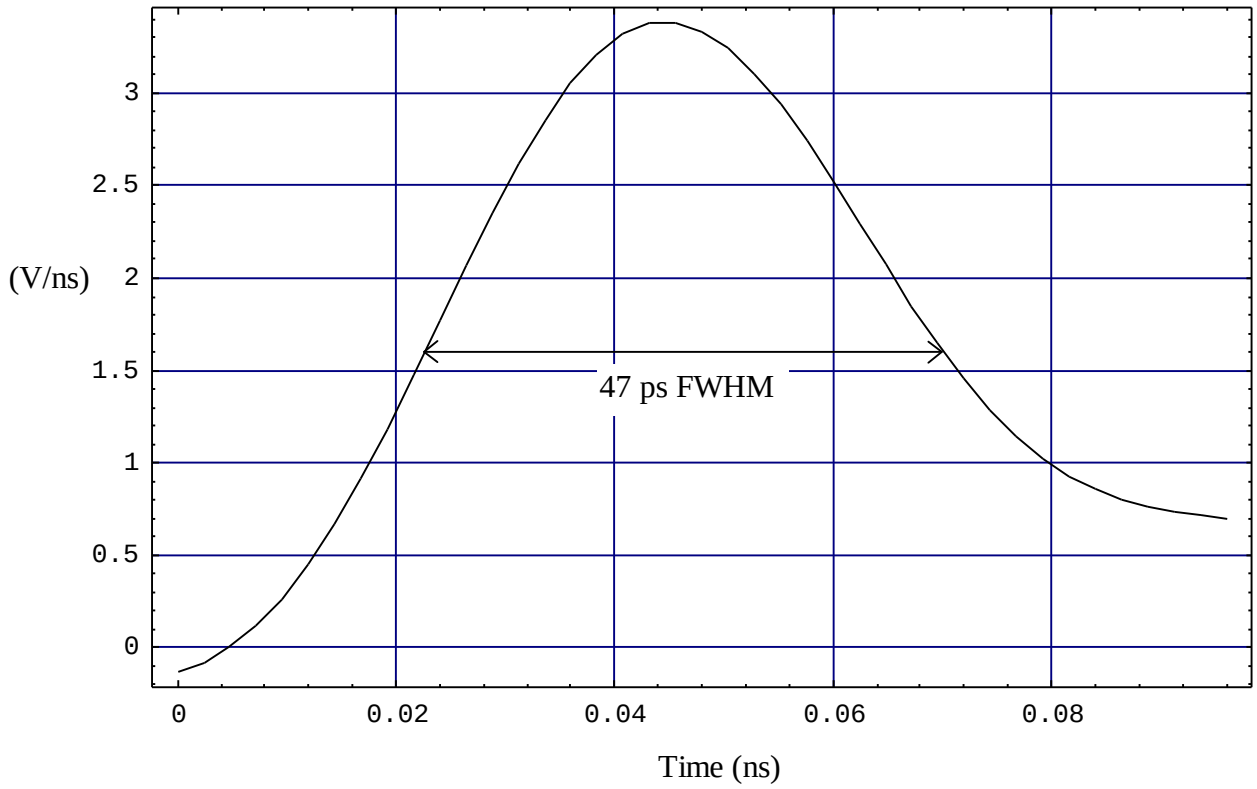

Figure 8.12. The derivative of the voltage reflected from the short after filtering.

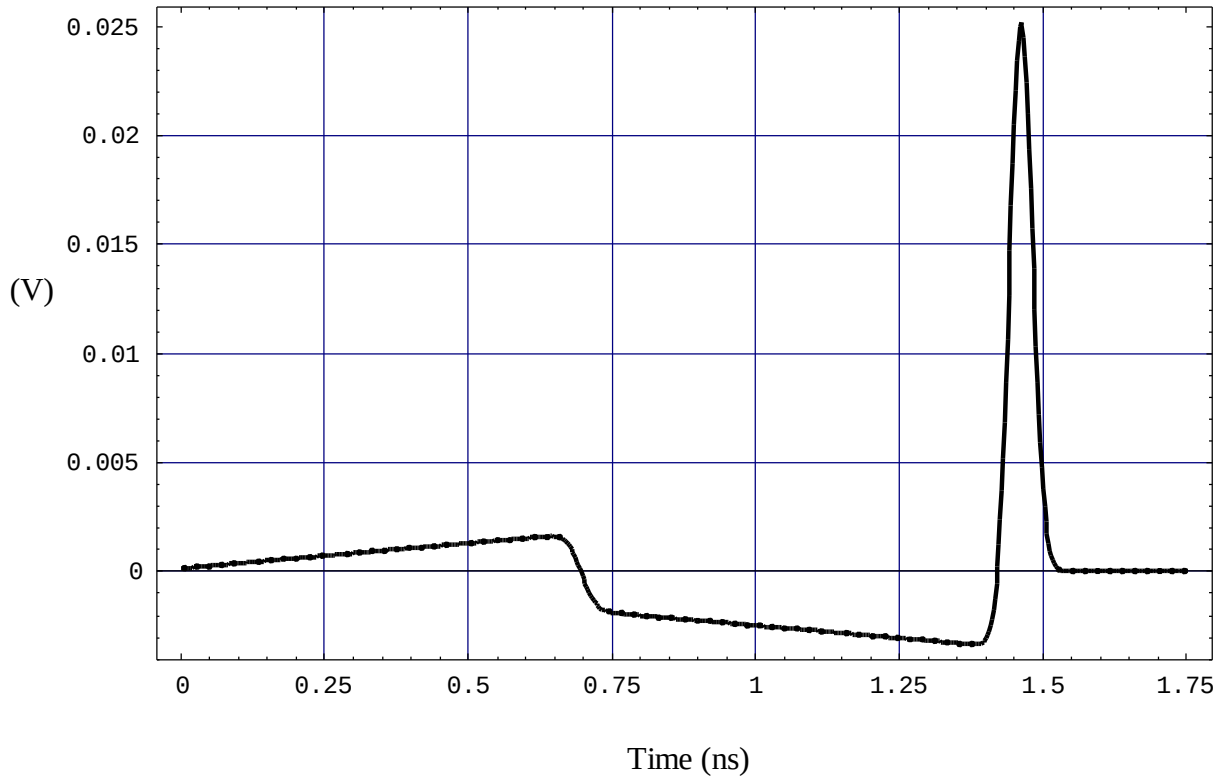

Figure 8.13. The predicted received voltage. (Compare to Figure 8.7.)

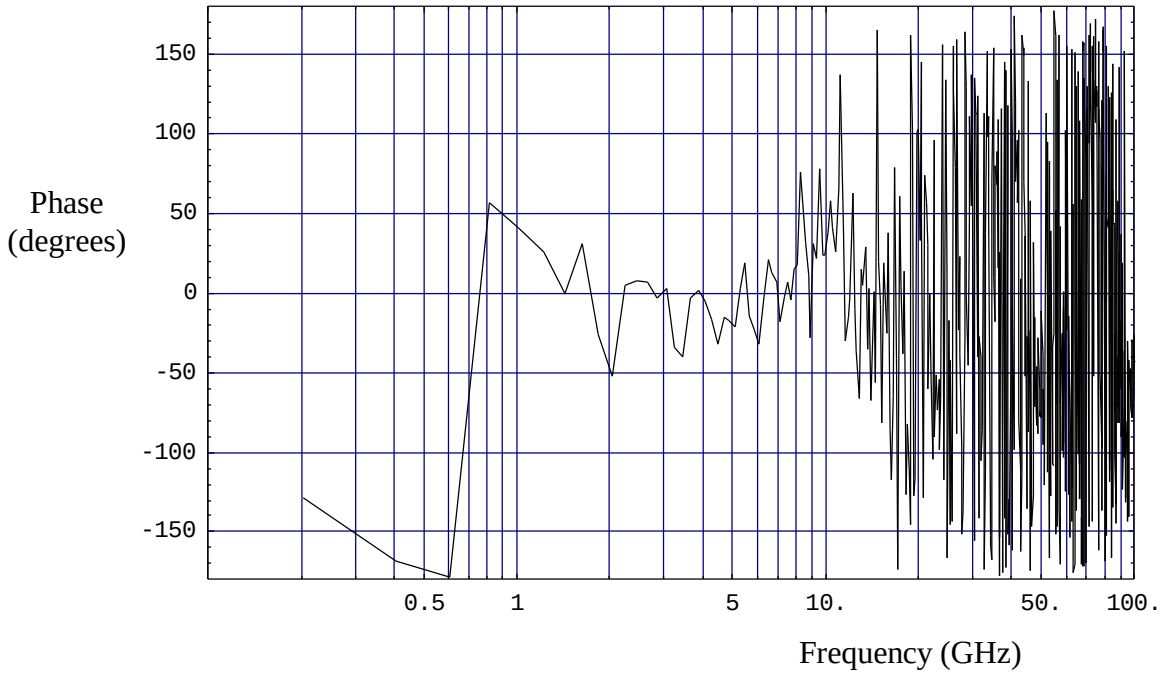

Figure 8.14. The phase of $h^2(\omega)/f_g$ after unwrapping, just before taking the complex square root.

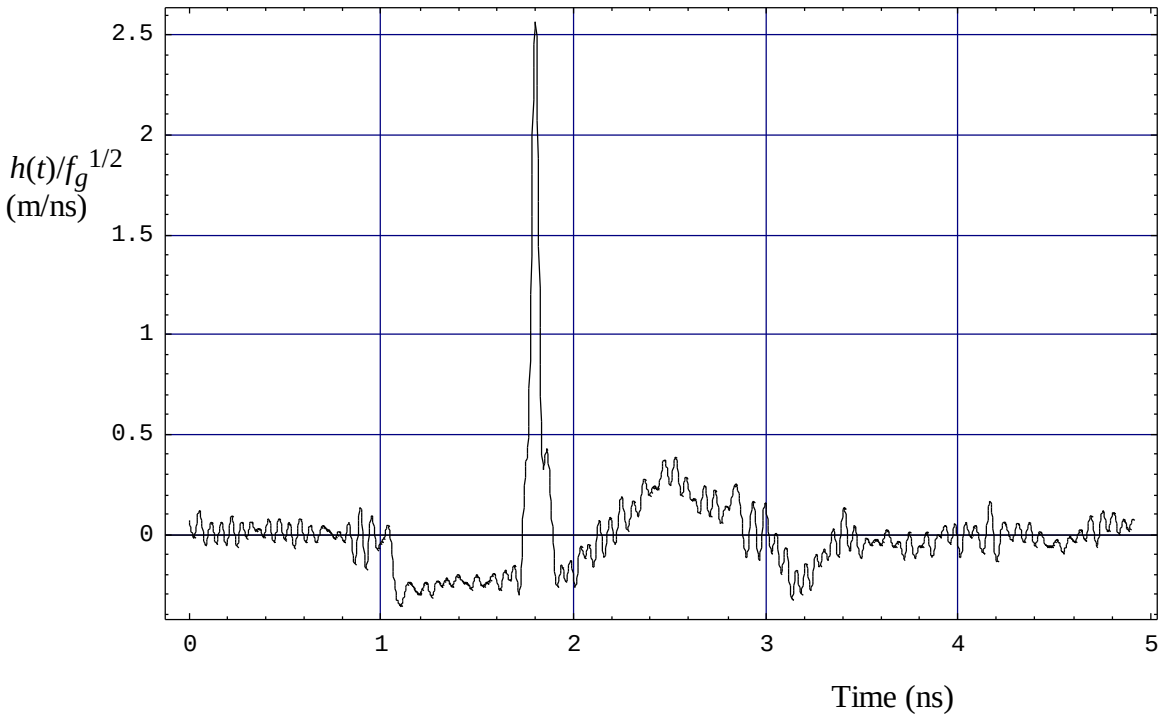

Figure 8.15. Normalized $h(t)$ for IRA-1, calculated from the measurement.

IX. Outdoor Antenna Measurement with Two Identical Antennas

A second experiment was performed to measure the performance of the IRA without the reflecting plate. While the technique with a reflecting plate is valid for small antennas, our antennas with 23 cm radius are too large to allow a convenient measurement in the far field. Furthermore, while the background subtraction method worked well in removing primary reflections, we were concerned that there could be secondary reflections in the confined indoor environment that could not be removed in processing. Finally, it will eventually be necessary to make measurements on the penetration of short impulses through slabs of lossy materials. For all these reasons, we made measurements outdoors with two identical antennas using a higher power source.

The test configuration is shown in Figure 9.1. The receiving antenna, sampling scope, and computer acquisition were located on a wooden platform. The receiving antenna (IRA-2) on its 1.2-meter tripod had a total height above the surrounding terrain of 4 meters. The 9-volt step pulser was located with the transmit antenna. The transmit antenna (IRA-1), also on a 1.2-meter tripod, was located on an uphill slope, giving a height above the intervening terrain of approximately 2.4 meters. This combination, together with the 9.1-meter antenna separation, gave approximately 5 ns of transit time isolation before the first reflected signal. Because of this large transit time isolation, background subtraction in the signal processing was not necessary.

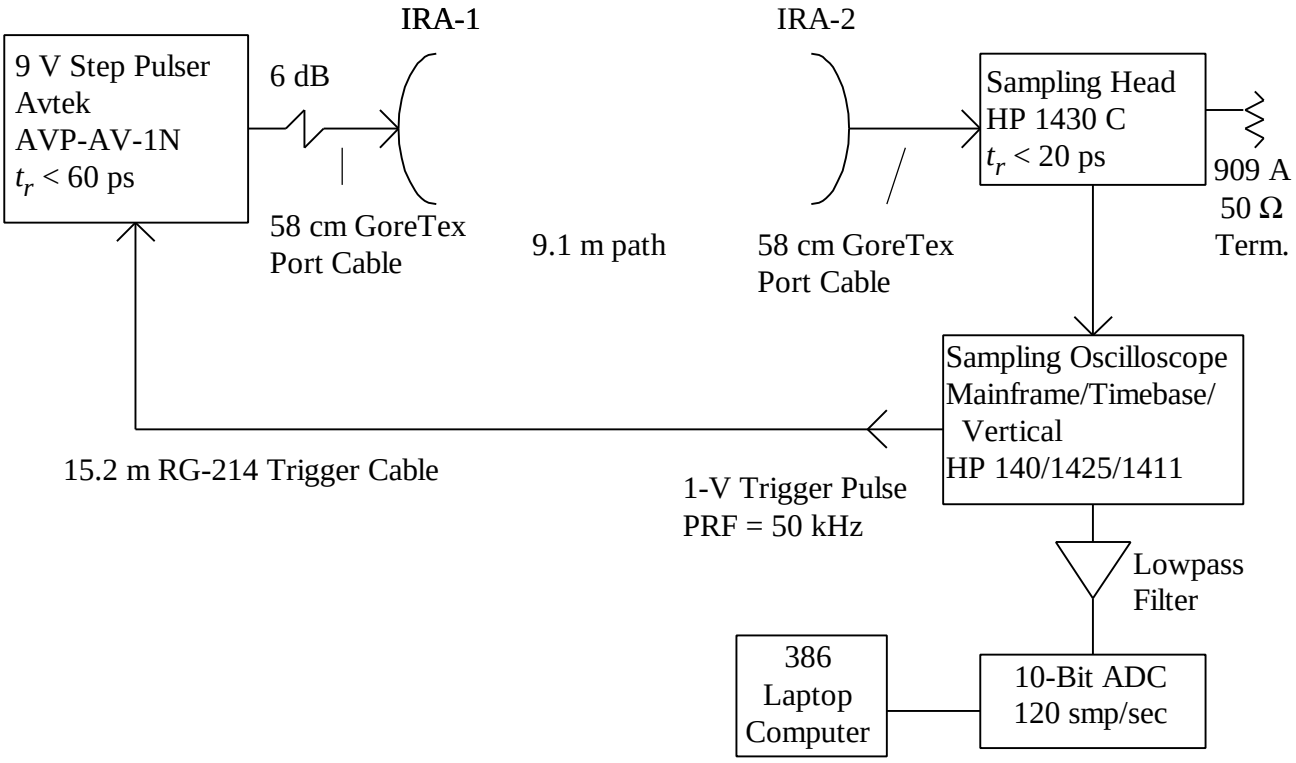

Figure 9.1. Outdoor Antenna Measurement Setup

The transmit and receive antennas (IRA-1 and IRA-2) were each 46 cm in diameter with $F/D = 0.25$ and with an integrated balun. The IRA-1 used as the transmit antenna was excited by the AVTEK model AVP-AV-1-N step pulse generator. This generator has variable amplitude and pulse width and can produce a step pulse up to 9 volts and a risetime < 60 ps. This level is approximately 50 times higher than the tunnel diode pulser used for the indoor test. The higher level gives much better signal-to-noise ratio for the outdoor test. A 6 dB 18 GHz attenuating pad (ARRA model 9412-6) was used to absorb back reflections from the antenna. A 58 cm length of Goretex microwave port cable transmitted the step pulse from the pulse generator to the antenna. This arrangement gave approximately a 4-volt signal at the antenna input connector. The AVTEK pulse generator was operated in a slave mode and was triggered by the 1 volt trigger output signal from the sampling oscilloscope through a 15.3 meter length of type RG-214 trigger cable.

The output from the IRA-2 receiving antenna was transferred through a 58 cm length of Goretex microwave port cable to the Hewlett Packard (HP) model 1430C sampling head, which had a risetime of less than 20 ps. The sampling head was controlled by an HP model 140 sampling oscilloscope mainframe with HP model 1425A sampling time base and HP model 1411A sampling vertical amplifier. The time base was operated in free run mode giving a pulse repetition frequency of 50 kHz. The trigger output from the time base triggered the AVTEK generator. The analog scope outputs from the sampling vertical amplifier were passed through a low pass filter to a 10 bit analog-to-digital converter (ADC) operated at 120 samples/sec. The analog-to-digital converter was controlled and recorded by the 80386 portable laptop computer, and the data was streamed directly to disk for later analysis. The HP140 sampling system was used rather than the portable HP182 TDR system used for the indoor test, due to equipment failure. The HP140 actually has superior performance, with a risetime of < 20 ps, but it is a heavy unit and difficult to transport. The complete system was calibrated as described in Section VII using a tunnel diode pulser to excite the 1.47 ns timing standard for timebase calibration, and a DC transfer standard for amplitude calibration. The antenna response was measured on 3 sweep speeds of 200 ps/div, 500 ps/div, and 1000 ps/div at 5 mV/div vertical sensitivity. A clean prepulse followed by a reverse polarity impulse of approximately 50 mV amplitude was observed.

The input signal was characterized by bringing the AVTEK pulse generator to the location of the sampling head and recording its signal attenuated by a 20 dB pad (ARRA model 9412-20). With this method both Goretex cables were in the loop. The calibration of the antenna relative to the input pulse thus compensated for both port cables, but not the baluns and cables internal to the antennas. Thus, with this method of calibration, we are including the balun as part of the antenna. In principle, we could use the data from Figure 7.6 to de-embed the effect of these cables. Although that was not done in this test, it will probably be necessary in future tests to obtain better agreement between theory and measurement. Since we are not including balun losses in our theory, we expect our theory to overestimate the received voltage somewhat.

The data and signal processing proceeded as follows. The source pulse waveform is shown in Figure 9.2. This is data taken at the faster sweep speed of 0.25 ps/sample. After filtering at 20 GHz with a 5th-order modified Butterworth filter, then taking the derivative, a

close-up of the impulse is shown in Figure 9.3. This impulse has a peak dV/dt of 61 V/ns, and a t_{FWHM} of 59 ps. If we fit an integrated Gaussian step function to these parameters, we find a peak magnitude of 3.5 V and a derivative risetime of 57 ps.

The source parameters are then used to predict the received voltage when the signal is passed through both antennas. The expected received voltage, with a correction for aperture blockage, is shown in Figure 9.4. This can be compared to the experimental received voltage in Figure 9.5. This is data is taken at a sampling rate of 0.46 ps/sample. Note that we are predicting reasonably well the magnitude and duration of the prepulse. On the other hand, the measured magnitude of the impulse is about 28% of what our model predicted.

Let us consider now whether our results are reasonable. First, we note that the signal passes through the antenna twice, so for one-way transmission we are measuring $0.28^{½} = 0.53$ times what we expect for a single pass through the antenna. Furthermore, we note that our prediction does not take into account cable losses in the balun, and we have shown in Section VII that cable losses are important. If we take cable losses into account, our measurement would be reasonably close to the predicted value. Note also that there appears to be a small amount of clipping in the raw received voltage in Figure 9.5, which also tends to reduce our measured values. Thus, given all these factors, we consider our agreement with the theory to be reasonable.

We now process the received voltage to obtain $h(t)/f_g^{½}$, using the processing techniques of Section III. The corresponding source voltage is shown in Figure 9.6, sampled at a rate of 0.46 ps/sample. This is essentially the same as Figure 9.2, but with a different sampling rate. Note that the polarity has been inverted for clarity. Before the complex square root can be taken, the phase must be properly unwrapped. This was accomplished using the time-shift technique described in Section III. The magnitude and phase of $h^2(w)/f_g$ are shown in Figure 9.7, just before the complex square root is taken. The phase is almost completely unwrapped, except for a single wrap at 600 MHz. We believe that this single phase wrap at low frequencies has little effect, but in future work we will implement a more complete algorithm to understand better its effect. Note that the mid-band phase plot is flat, and that phase wraps at high frequencies are unimportant because the magnitude there is small.

After taking the complex square root and converting to the time domain, the resulting $h(t)/f_g^{½}$ is shown in Figure 9.8, and a closeup of the peak is shown in Figure 9.9. The overall shape is close to what we expect, i.e., a prepulse followed by an impulse. Based on equations (2.1-2.2), we expect the duration of the prepulse to be 770 ps, and that is about what we observe. We expect the magnitude of the prepulse to be 0.27 m/ns, and we observe about half that. The impulse area is predicted to be 0.206 m, and we observe an area of 0.14 m. Thus, our calculated impulse area is 68% of the predicted value. If we include balun cable losses in our theory, that would reduce our theoretical values, so our measurements would be quite close. The full width half max of the impulse is 36 ps. Theoretically, the width of a delta function is zero, but real devices always have a finite risetime. Our results suggest that the risetime of the antenna (including the balun) is 36 ps, which is quite satisfactory for our purposes.

Finally, it may be of interest to calculate the radiated electric field on boresight when the antenna is driven by an ideal step-function voltage with a risetime of zero. This is the best possible radiated field one can get out of the antenna. It is obtained from equation (2.1) by using a driving voltage of $V_o\, u(t)$ on the 50-ohm feed line. Thus, we have an optimized radiated field $E^{opt}(t)$ of .

$$E^{opt}(t) \;=\; \frac{V_o}{r}\,\frac{\sqrt{2}}{p\,c\,f_g}\,h(t) \tag{9.1}$$

Note that we have taken into account the balun and the second pair of arms by including an additional factor of $2\sqrt{2}$ in the above equation. Note also that the f_g factor refers to the normalized impedance of a single pair of arms (f_g = 400Ω/377Ω = 1.06)

We implemented the above scaling of the measured $h(t)$ to obtain the radiated field for a 1-volt perfect step driving function, scaled to a one-meter distance. The result is shown in Figure 9.10. One can use this to compare to other antennas for those situations where the pulser has a risetime much faster than the risetime of the antenna. Finally, photos of the test site are shown in Figures 9.11 and 9.12.

The results of the outdoor test were in good general agreement with the expected theoretical results. Cable losses appear to be the dominant loss mechanism, and future work can take this into account better by using the measurements of Section VII. Cable losses would be reduced by placing the source and sampler at the antenna apex, or by using a larger diameter cable. Note, however, that larger cables may have difficulty maintaining the risetime through bends in the cable. Also, it is more difficult to build a small geometry at the feed point with larger cables. Thus, it is clear that some tradeoffs in cable size will have to be made.

In summary, we note that the step response of the antenna, $h(t)$, has a pulse width of just 36 ps. This is considerably faster than the 100 ps or so that we set out to achieve, so we consider the test to be quite successful.

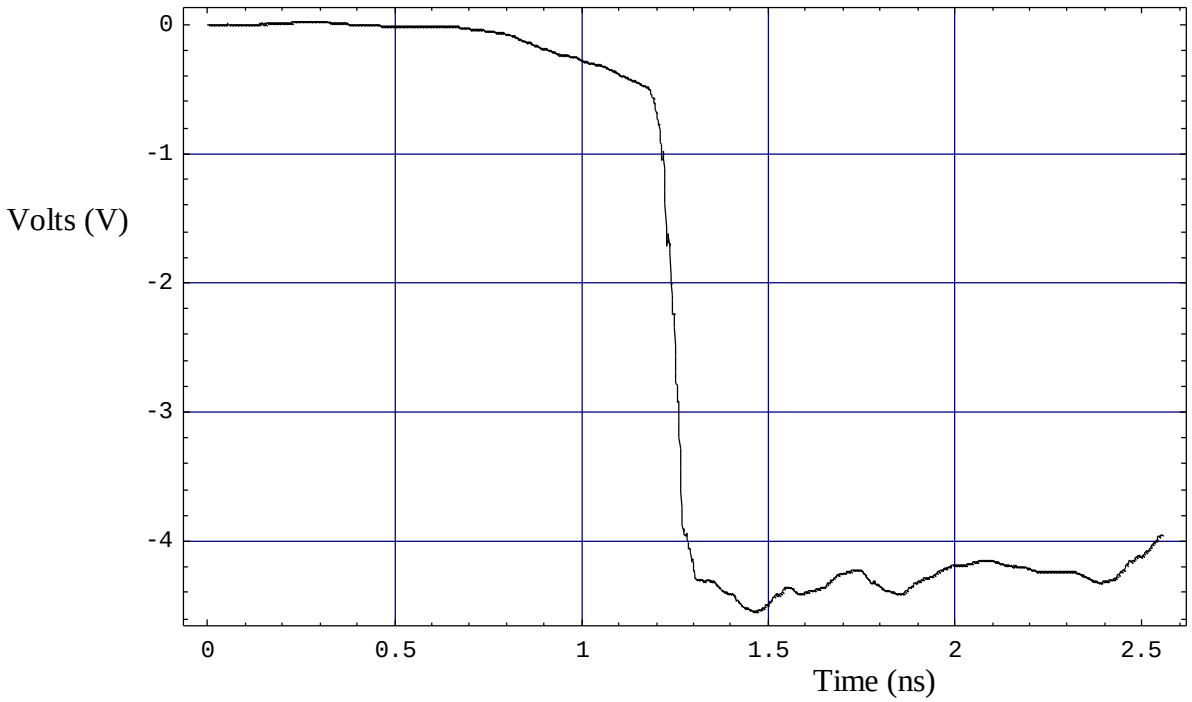

Figure 9.2. The source voltage, taken at a sweep speed of 0.25 ps/sample.

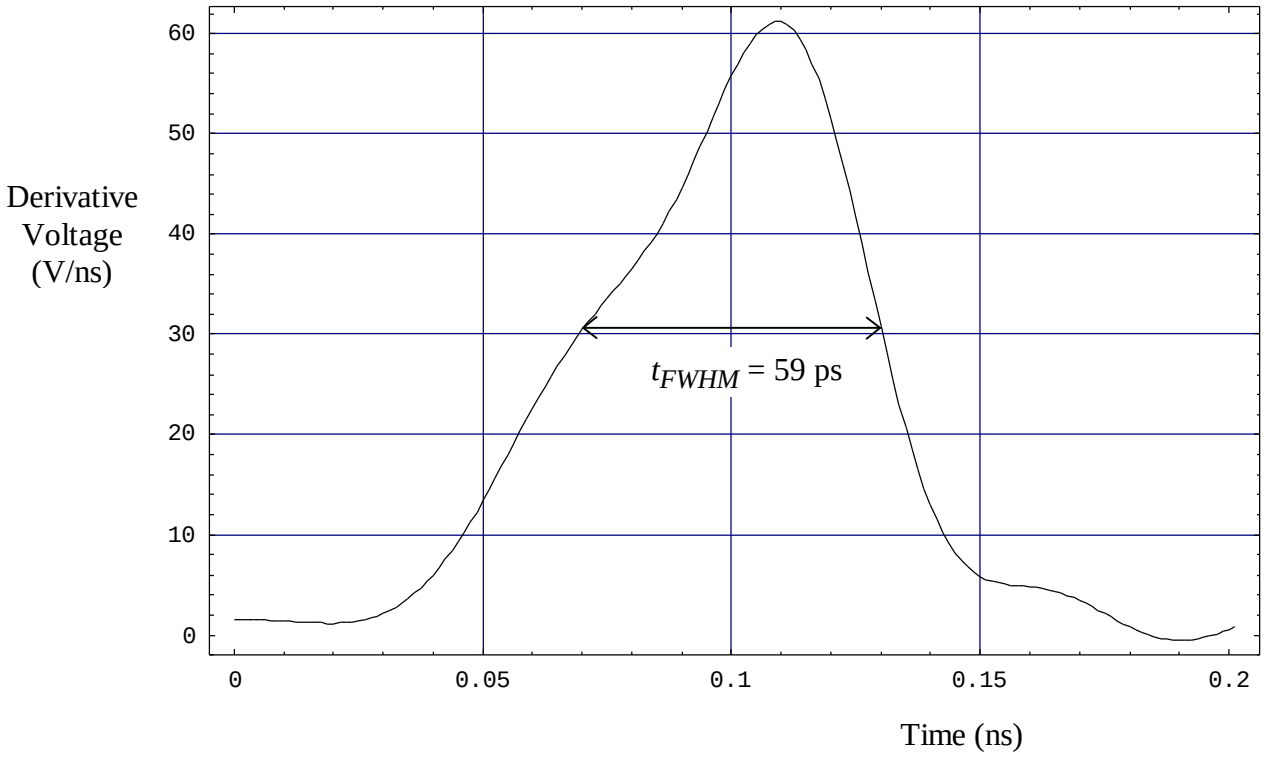

Figure 9.3. The derivative of the source voltage, after filtering and taking the derivative.

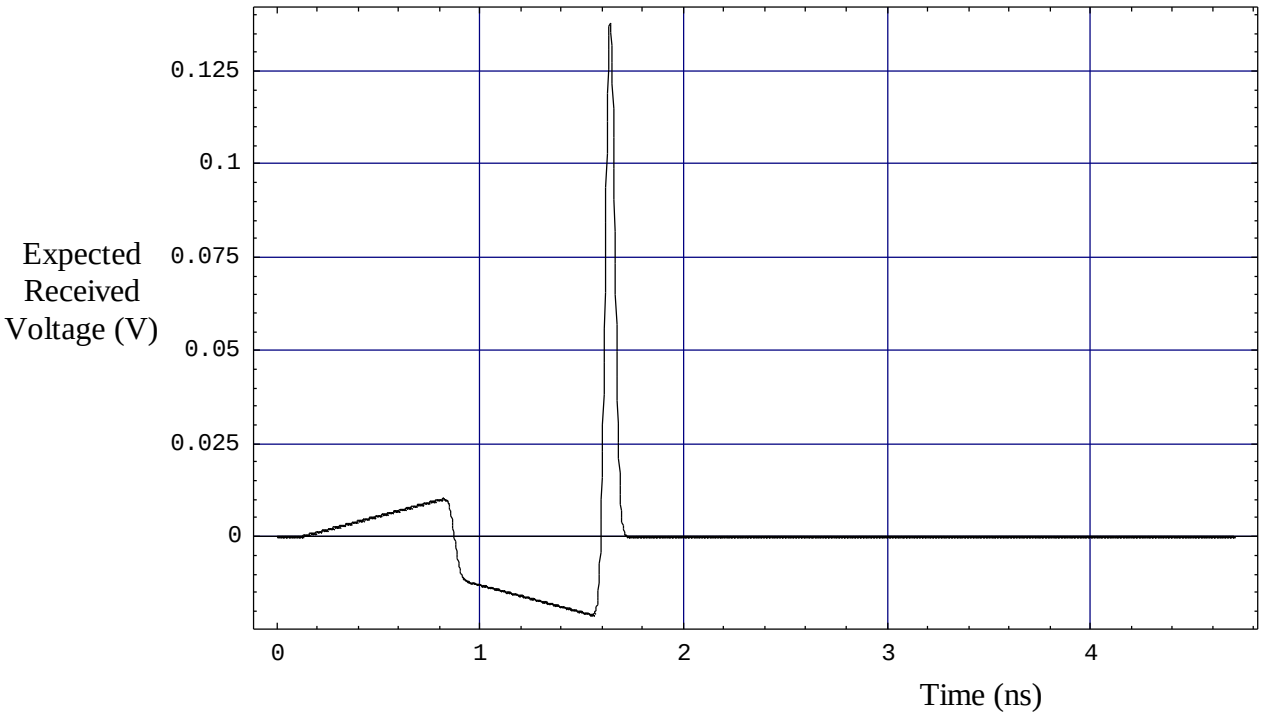

Figure 9.4. Expected received voltage.

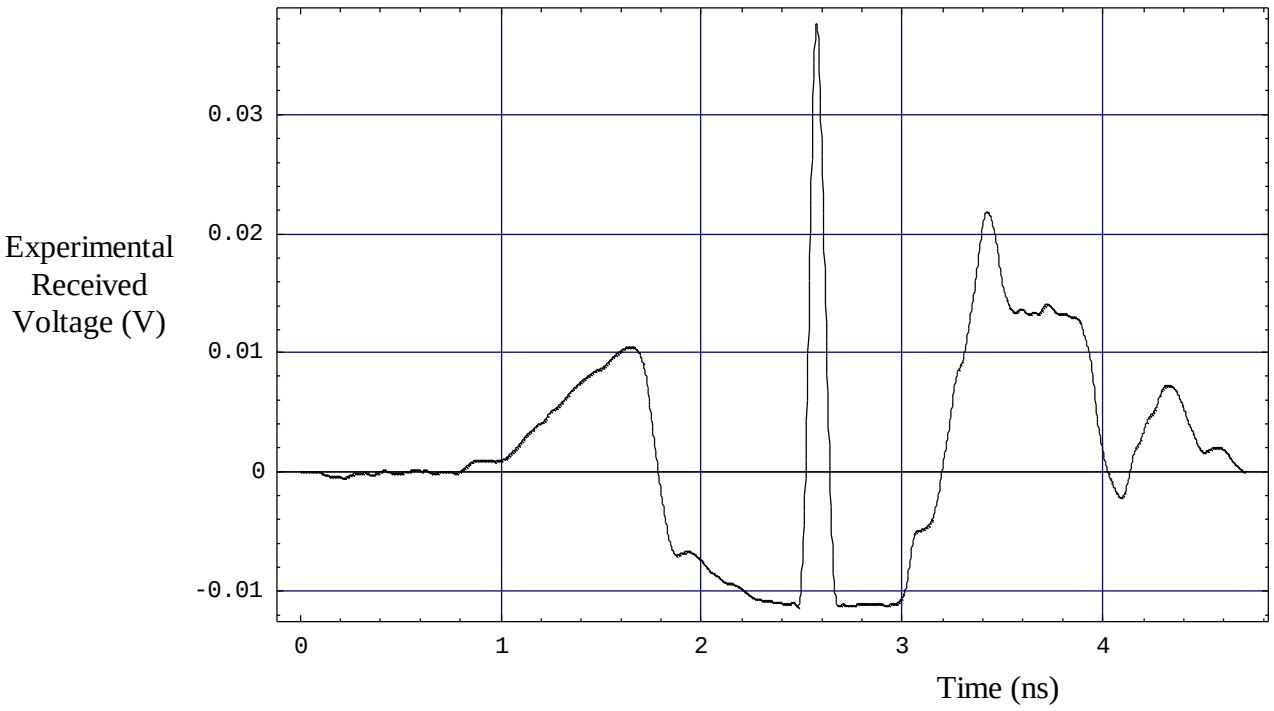

Figure 9.5. Experimental received voltage.

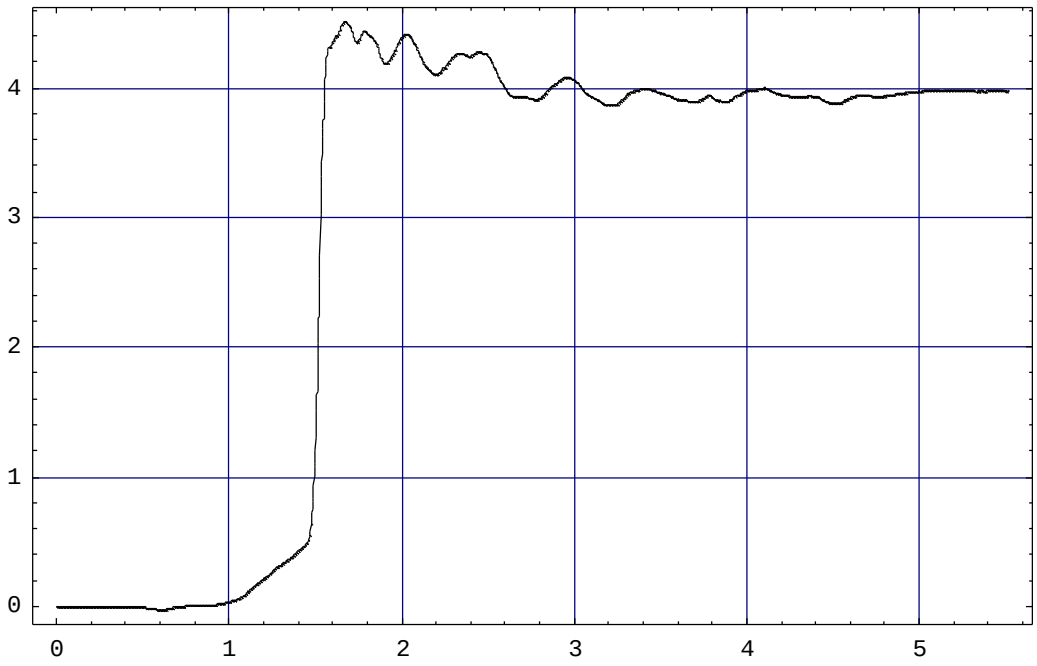

Figure 9.6. The source voltage sampled at 0.46 ps/sample.

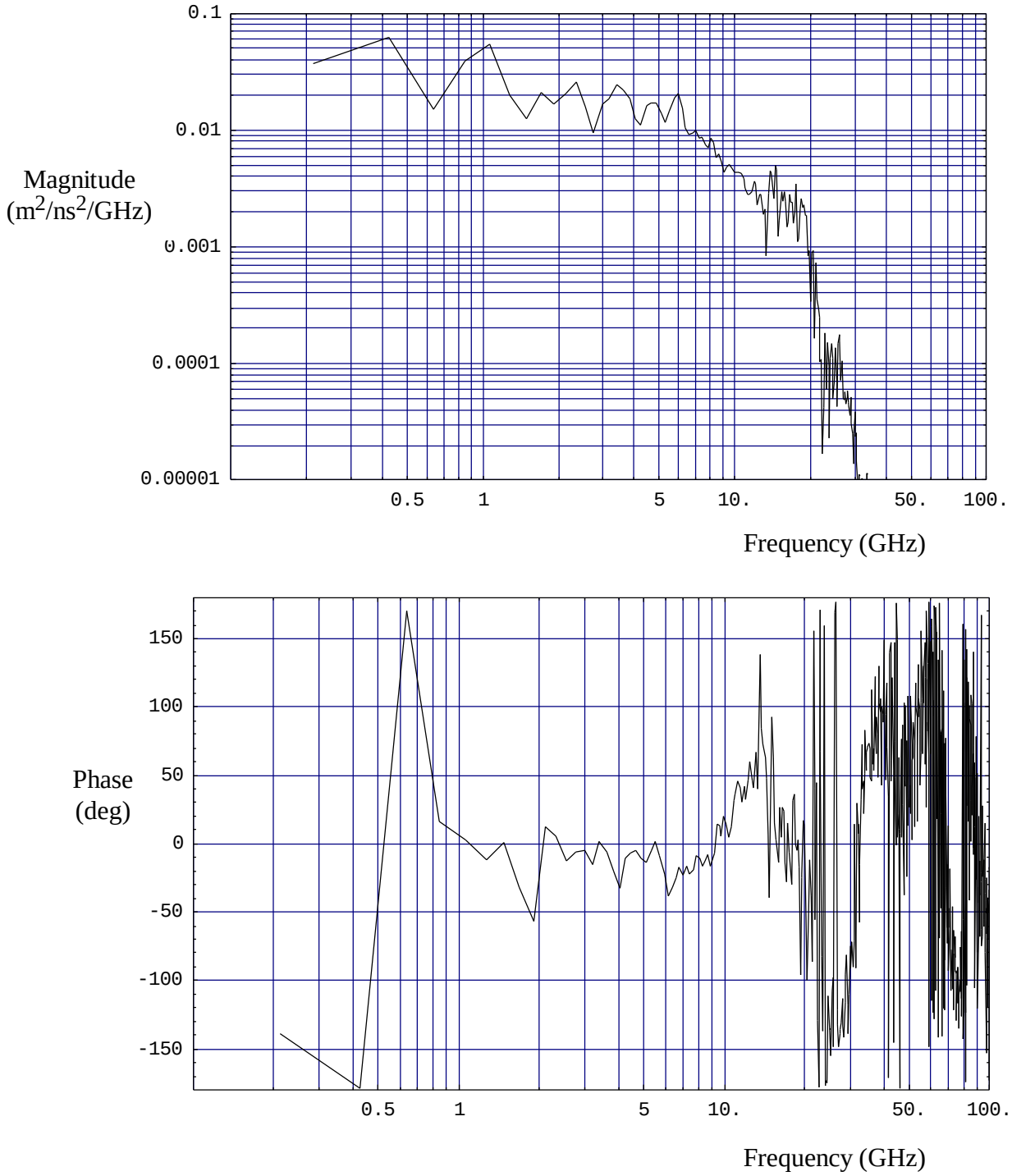

Figure 9.7. The phase-unwrapped $h(w)^2/f_g$ in the frequency domain, just before taking the square root and converting to the time domain.

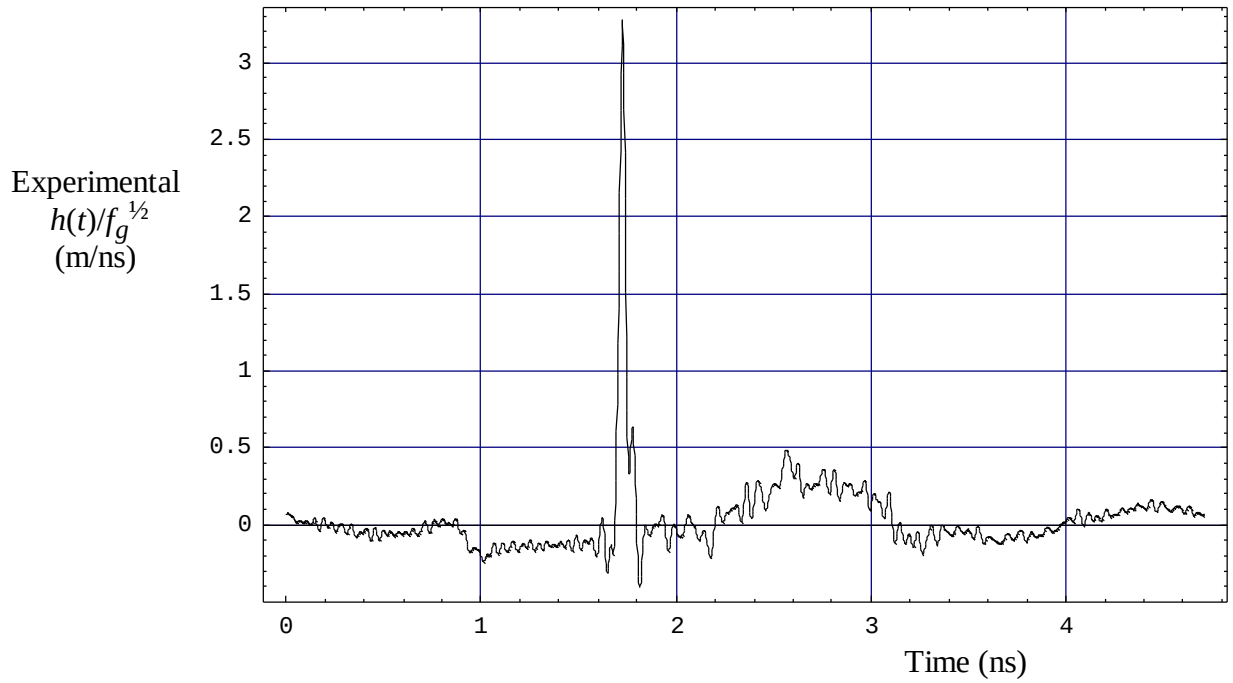

Figure 9.8. Processed $h(t)/f_g^{½}$.

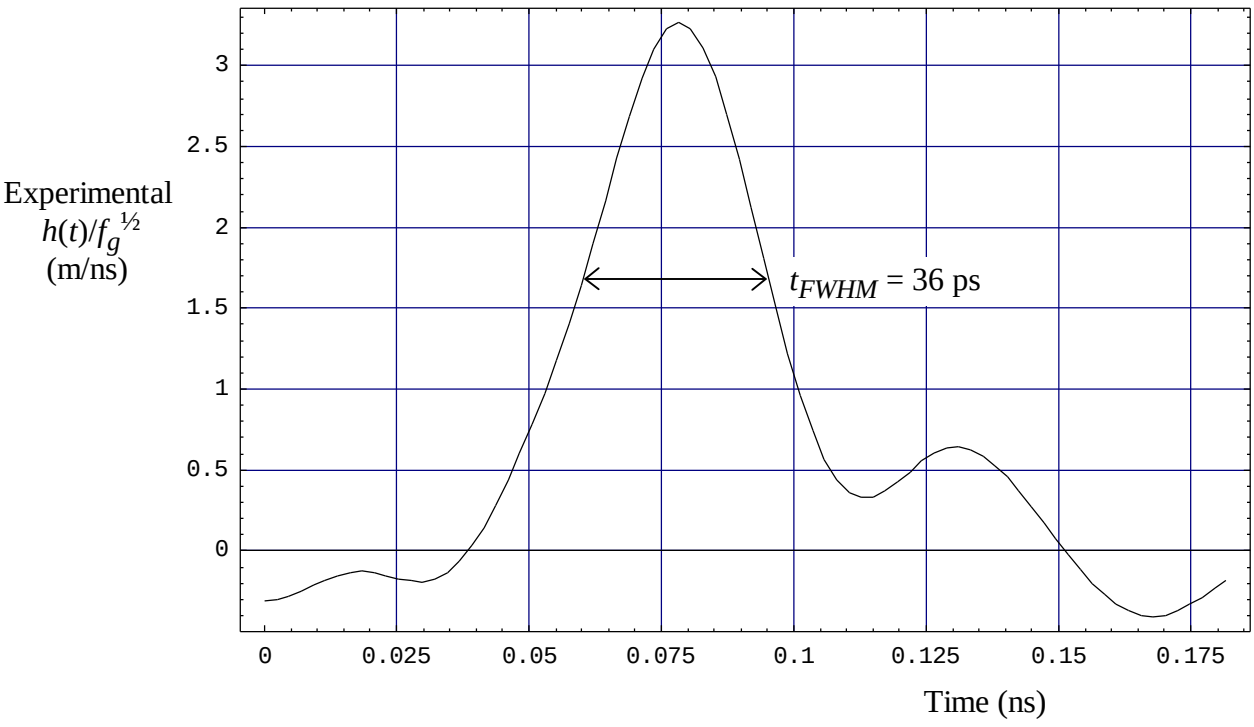

Figure 9.9. Close-up of the peak of Figure 9.8.

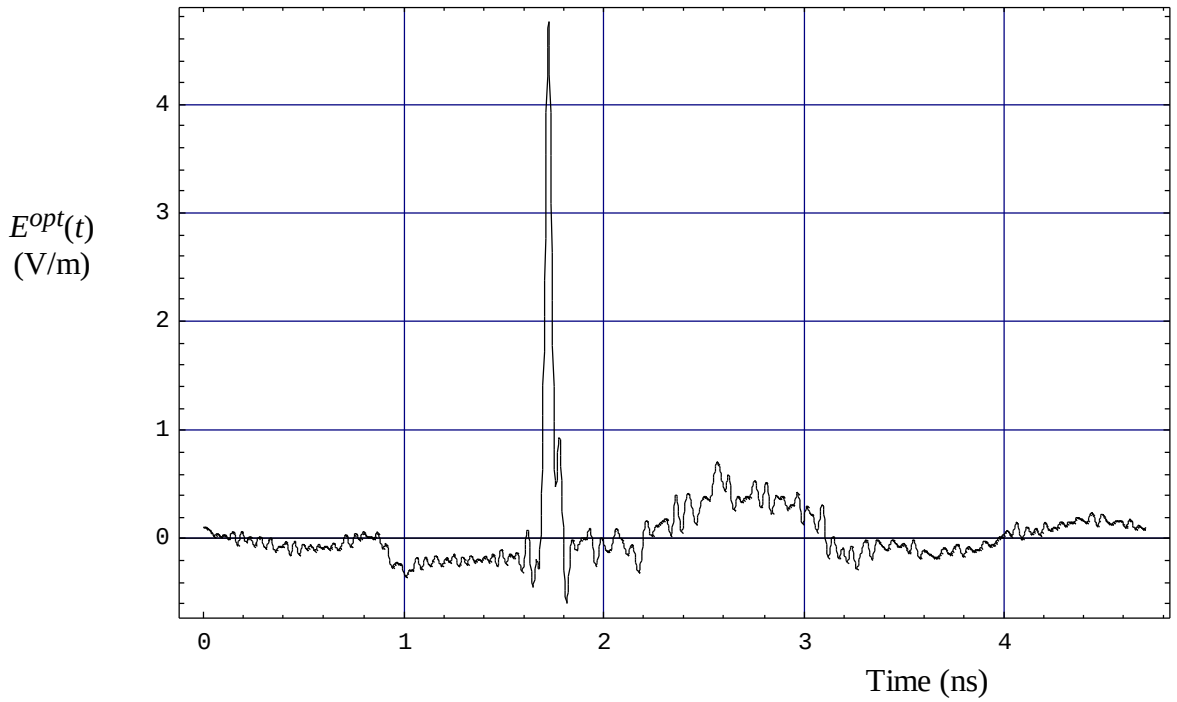

Figure 9.10. A rescaling of Figure 9.8 to allow one to predict the field radiated by the antenna scaled to a 1 meter distance, when excited by a 1 V step pulse with infinitely fast risetime.

Figure 9.11. The receiving IRA at the outdoor test location.

Figure 9.12. The outdoor test site, showing both the receiving IRA (foreground), and the transmitting IRA (behind Dr. Frost).

X. Propagation Theory

In order to understand Ground Penetrating Radars (GPRs), it is critical to understand the propagation properties of the media in which the radar will operate. Toward this end, we present an initial survey of the methods available for predicting pulse propagation through frequency-dependent dielectric media. We consider here both analytical methods and methods based on experiments. In Section XI, we summarize briefly some numerical methods based upon the Finite Difference Time Domain (FDTD) method. In Section XII, we propose experimental methods for measuring material properties.

A. Analytic Methods

A number of models of dielectric material are available. In the frequency domain, one can express the relative permittivity as

$$e(w) = e_o\left[e_\infty + X(w)\right] \tag{10.1}$$

where e_∞ is the relative permittivity at infinite frequency, and $X(w)$ is the frequency dependent portion of the relative permittivity. Various models can be used to express the frequency-dependent portion of the relative permeability. The most commonly used (and simplest) is the Debye model, which uses a single pole, and has the form [8]

$$X(w) = \frac{e_S - e_\infty}{1 + jw\,t} \tag{10.2}$$

Thus, the permittivity is dependent only upon a single relaxation time t, a static (low-frequency) permittivity e_S, and a high-frequency permittivity e_∞. As an example, the complex dielectric constant of water is plotted as a function of frequency in Figure 10.1

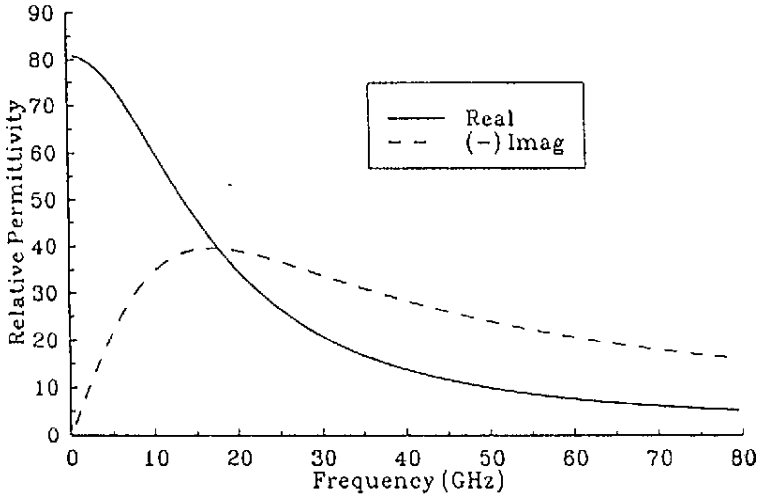

Figure 10.1. Complex relative permittivity of water (from [8])

In the time domain, to get $D(t)$ from $E(t)$, one convolves the electric field $E(t)$ with the permittivity. Thus, we have

$$\begin{aligned} D(t) &= e_o\left[e_r(t) \circ E(t)\right] \\ &= e_o\left[e_\infty d(t) + X(t)\right] \circ E(t) \end{aligned} \tag{10.3}$$

where the " ° " symbol indicates a convolution, and $d(t)$ is a Dirac delta function. If we convert the relative permittivity to the time domain, we find the frequency-dependent portion of the response of a Debye medium to an impulse is just a simple decaying exponential, or

$$X(t) = \frac{e_s - e_\infty}{t} e^{-t/t}\ u(t) \tag{10.4}$$

where $u(t)$ is the Heaviside step function. Note that the Debye model has a particularly simple inverse Laplace transform. Other models are either more complex, or simply do not have an analytic inverse transform.

Let us consider now some of the other forms for the frequency dependent dielectric constant that have been used in the past. The simplest modification is to use a sum of exponentials for $X(t)$ [9,10]. This would normally be expressed as

$$X(t) = \left[\sum_{n=1}^{N} a_n e^{-b_n t}\right] u(t) \tag{10.5}$$

where the a_n's and b_n's are positive real numbers. Of course, this has simple inverse transform

$$X(s) = \sum_{n=1}^{N} \frac{a_n}{s + b_n} \tag{10.6}$$

This is actually a specific form of a more general rational function

$$X(s) = \frac{\sum_{m=0}^{M} A_m s^m}{\sum_{n=0}^{N} B_n s^n}\ , \qquad N > M \tag{10.7}$$

The form in eqn. (10.6) has been developed in some detail in [9], and it corresponds to a specific type of RC ladder network. Further details can be found in [9].

Let us consider now how one might use these frequency-dependent dielectric constants to solve a one-dimensional propagation problem. We propose first to consider a simple uniform medium and plane-wave propagation. For this case, the electric field must satisfy a Helmholtz equation

$$\frac{\partial^2 E}{\partial z^2} - \gamma^2 E = 0$$
$$\gamma = \frac{jw}{c}\sqrt{\varepsilon_r(w)} \tag{10.8}$$

Although we must revert back to the time domain eventually, it happens to be easier to solve the problem in the frequency domain, and convert back to the time domain later.

This formulation allows propagation through one-dimensional layers, as shown in Figure 10.2. This is analytically tractable through any number of layers necessary. One would solve the problem at each frequency, and then convert back to the time domain.

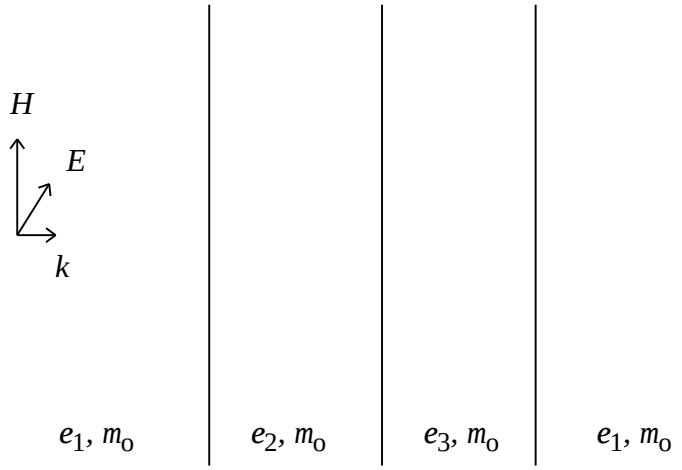

Figure 10.2. Propagation through layers.

This technique can be extended to non-plane-wave propagation by taking the Fourier transform of the Helmholtz equation in the x and y directions. First we express the Helmholtz equation in three dimensions as

$$\frac{\partial^2 E}{\partial x^2} + \frac{\partial^2 E}{\partial y^2} + \frac{\partial^2 E}{\partial z^2} - \gamma^2 E = 0$$
$$\gamma = \frac{jw}{c}\sqrt{\varepsilon_r(w)} \tag{10.9}$$

Next, we note that if we take the Fourier transform in the x and y directions, the derivatives with respect to x and y become simply jk_x and jk_y, respectively. This results in

$$\frac{\partial^2 E}{\partial z^2} - \Gamma^2 E = 0$$
$$\Gamma = \sqrt{g^2 + k_x^2 + k_y^2} \tag{10.10}$$

The solution process would begin by expressing an aperture electric field at $z = 0$, taking its Fourier transform in the x and y directions, and propagating the result through the layers in the frequency domain. While this is analytically tractable, the three-dimensional Fourier transform (two space dimensions and one time dimension) may be difficult to implement in practice. If the problem is circularly symmetric, as would be the case for uniform excitation over a circular patch at $z = 0$, then one would need only a two-dimensional transform, and the problem would become more manageable.

B. Methods Based on Experiments

An equivalent way of thinking about the relaxation time is to actually look at a TDR of the reflection of a step-function voltage from an air/dielectric interface. Sample measurements using this technique were carried out in [11]. An example TDR is shown in Figure 10.3. From this reflection, one can see clearly the low- and high-frequency limits of the reflection coefficient, and the relaxation time. It is simple to convert these reflection coefficient limits to dielectric constants, so one then has all the relevant information to fit the Debye model of equation (10.2).

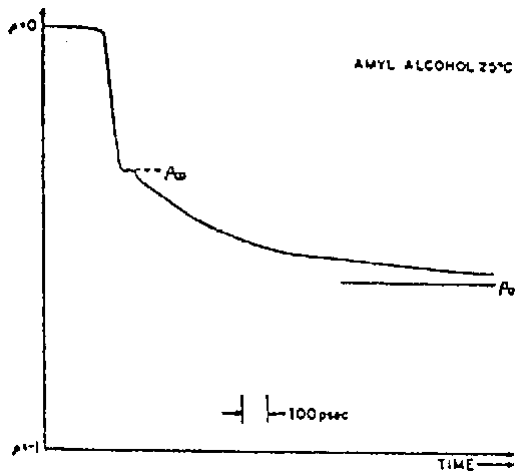

Figure 10.3. Sample TDR (reflection coefficient vs. time) for a reflection from Amyl Alcohol; from [11].

Some sample data from the Fellner-Feldegg study [11] (Figure 10.4) plots the relaxation times for several alkyl alcohols as a function of temperature. Notice that relaxation times of a few tens of picoseconds to a hundred nanoseconds were obtained. Relaxation times, as well as complex permittivity values obtained in the study of organic liquids, compared well with literature values obtained by more traditional techniques. The parameters of the media were obtained over

a larger frequency than would be possible with a frequency domain technique. Note that in this study, it was necessary to use models more complex than the simple Debye model. This points out the importance of having some flexibility to apply a variety of different models to the measured data.

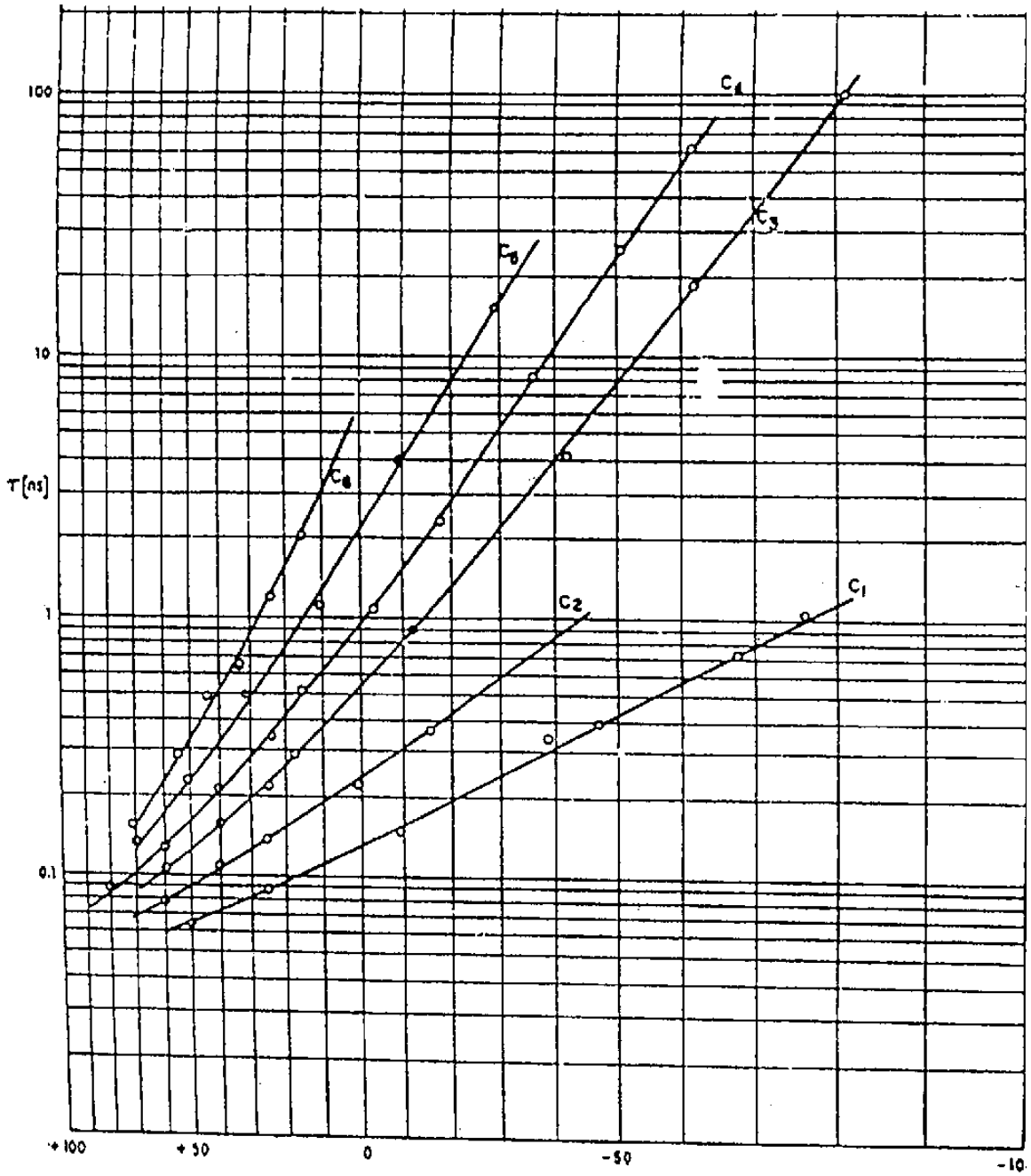

Figure 10.4. Relaxation time as a function of temperature (degrees C) for various alkyl alcohols, from [11].

XI. Frequency-Dependent Finite Difference Time Domain Techniques

We have shown that propagation through layers of media with frequency-dependent permittivities is solvable in closed form. If one is faced with a more complex geometry, however, a numerical method will be required. We consider here how to apply a Finite-Difference Time Domain (FDTD) algorithm to a simple Debye medium. We also consider how this might be extended to other media. Although we consider here only a 1-dimensional problem, the method can be extended to two and three dimensions.

We begin with Maxwell's equations in the time domain. Thus we have,

$$\begin{aligned} \nabla \times \overline{E} &= -m_o \frac{d\overline{H}}{dt} \\ \nabla \times \overline{H} &= \frac{d\overline{D}}{dt} + s\,\overline{E} \\ D(t) &= e_o\left[e_r(t) \circ E(t)\right] \end{aligned} \tag{11.1}$$

We can specialize these equations to one dimension, assuming that waves propagate in the x direction, so

$$\begin{aligned} \frac{dH_z(x,t)}{dt} &= -\frac{1}{m}\frac{dE_y(x,t)}{dx} \\ \frac{dD_y(x,t)}{dt} &= -\frac{dH_z(x,t)}{dx} - s\,E_y \\ D_y(t) &= e_o\left[e_r(t) \circ E_y(t)\right] = e_o\left[e_\infty\, d(t) + X(t)\right] \circ E_y(t) \end{aligned} \tag{11.2}$$

It is simple now to convert the first two equations to an FDTD equation. We follow the development of [8] here. Thus,

$$\begin{aligned} {H_z}^{n+½}(i+½) &= {H_z}^{n-½}(i-½) - \frac{\Delta t}{m\,\Delta x}\left[{E_y}^{n}(i+1) - {E_y}^{n}(i)\right] \\ {D_y}^{n+1}(i) &= {D_y}^{n}(i) - \frac{\Delta t}{\Delta x}\left[{H_z}^{n+½}(i+½) - {H_z}^{n+½}(i-½)\right] - s\,\Delta t\,{E_y}^{n+1}(i) \end{aligned} \tag{11.3}$$

where the superscript n refers to the time step, and the index i refers to the position in the z direction. The constitutive relation is expressed as a convolution, i.e.,

$$D(t) = e_\infty e_o\,E(t) + e_o\int_0^t E(t-\Lambda)\,c(\Lambda)\,d\Lambda \tag{11.4}$$

which can then be discretized as

$$
\begin{aligned}
D^n &= e_\infty e_o E^n + e_o \sum_{m=0}^{n-1} E^{n-m} X^m \\
X^m &= \int_{m\Delta t}^{(m+1)\Delta t} X(\Lambda)\, d\Lambda
\end{aligned}
\tag{11.5}
$$

One can combine (11.5) with (11.2) by considering the expression for the difference in D between two consecutive time steps, i.e. $D^{n+1}(i) - D^n(i)$. After some calculation, and substituting into (11.3), one finds [8]

$$
\begin{aligned}
E_y{}^{n+1}(i) &= \frac{e_\infty}{\frac{s\,\Delta t}{e_o} + e_\infty + X^o} E_y{}^n(i) \\
&+ \frac{1}{\frac{s\,\Delta t}{e_o} + e_\infty + X^o} \sum_{m=0}^{n-1} E_y{}^{n-m}(i)\,\Delta X^m \\
&- \frac{\Delta t}{\frac{s\,\Delta t}{e_o} + e_\infty + X^o} \frac{\left[H_z{}^{n+\frac{1}{2}}(i+\tfrac{1}{2}) - H_z{}^{n+\frac{1}{2}}(i-\tfrac{1}{2})\right]}{e_o\,\Delta x} \\
\Delta X^m &= X^m - X^{m+1}
\end{aligned}
\tag{11.6}
$$

This is now sufficient, in combination with (11.3), to calculate a one-dimensional frequency-dependent FDTD problem. The extension to two or three dimensions is straightforward.

There is a difficulty, however, in the above relationship. The convolution in the second line of equation (11.6) is time-consuming to calculate, and it can also require considerable memory in a three-dimensional problem to store old values of E. For some media models, such as that for Debye media or for a sum of exponentials, the convolution at a given time is simply expressible in terms of the convolution at an earlier time step. Examples of these recursion relationships are provided in [8]. For other media, one must carry out the complete convolution at each time step, storing the old values of E_y for later use.

A more general technique for discretizing the constitutive relation is to use the so-called "derivative" formulation, as described in [8]. This is best illustrated by an example. Assume we must discretize the Debye constitutive relation, i.e.,

$$
e(w) = \frac{D(w)}{E(w)} = e_o\left[e_\infty + \frac{e_s - e_\infty}{1 + j w\, t_o}\right] \tag{11.7}
$$

This is rearranged as

$$(1 + jw\, t_o)\, D(w) \;=\; jw\, t_o e_o e_\infty E(w) + e_o e_s E(w) \tag{11.8}$$

Noting now that the operator jw is equivalent to a derivative in the time domain, this can be expressed as

$$D(t) + t_o \frac{\P D}{\P t} \;=\; e_o e_\infty t_o \frac{\P E}{\P t} + e_o e_s E(t) \tag{11.9}$$

This can then be discretized in the usual manner to calculate find E^{n+1} if one knows D and E at earlier time steps. Thus, we see that the third equation of equation (11.2) can be discretized directly, without a convolution, in certain cases.

It is apparent that there are several alternatives for addressing the problem of frequency-dependent propagation numerically. First, one has the option of looking for an efficient recursion relationship for the convolution in equation (11.6). Second, one might implement the constitutive relation with a derivative relationship such as that in equation (11.8). Finally, if no recursion or derivative relationship is available, and if the problem size is small enough, it may also be possible to carry out the convolution in (11.6) by brute force, storing the old values of the E-field for later use.

XII. Propagation Experiments

We outline here the methods that could be used to characterize frequency-dependent dielectric media. To measure the characteristics of various dielectric materials, we will use a method similar to the TDR reflection measurement of Ref. [11].

A diagram of our proposed experimental test setup is shown in Figure 12.1. This is very similar to the TDR antenna calibration method which was performed in Section VII, and the same basic equipment is used. A 20 ps step pulse is generated by the tunnel diode pulser. It is passed through the sampling head to a conical wave expansion section which allows an increase of the coaxial transmission line diameter to a convenient size, without exciting non-TEM modes. The wave propagates along the air-filled coaxial line to a planar interface with the lossy dielectric material. A reflection from the interface travels back to the feedthrough sampling head and is sampled with a 20 ps risetime unit, digitized by the 16-bit ADC, and recorded in the computer. It is necessary that the material-filled line have sufficient length that relaxation occurs before the reflection from the short at the end of the line. The reflection from the short then passes back through the dielectric to the sampling head. An analysis of the second reflection, which has passed through the dielectric twice, gives an independent measure of the transmission properties of the dielectric. Thus, we can measure both reflection and transmission characteristics with the same apparatus.

One can also install a second wave compression cone on the right hand side of the lossy media, in order to look at the transmitted signal directly, without reflecting from a short at the end of the line.

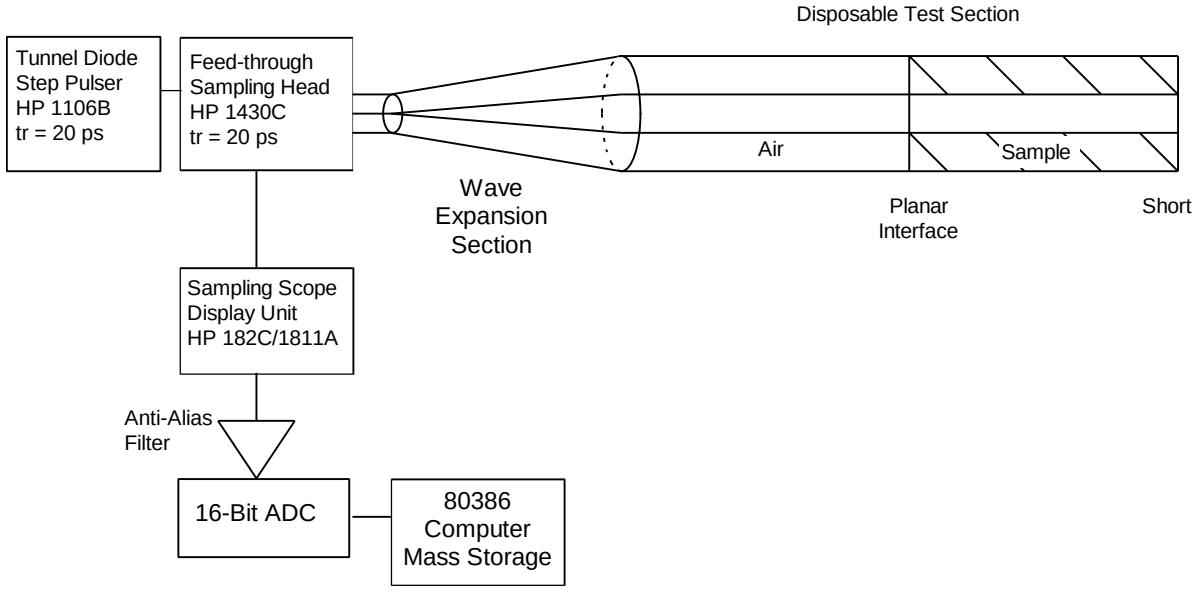

Figure 12.1. Experimental setup for lossy materials characterization.

For some materials which possess structure or orientation, such as rebar-filled concrete, it would be more appropriate to perform measurements using freely propagating waves from the impulse antennas. Small IRA antennas with a 20-cm diameter would be well suited to this task, because they generate short pulses with high gain. The experimental setup for this measurement would be the same as for the antenna measurements of Section X, with a slab of dielectric between the two antennas.

XIII. Conclusions

We have described here a variety of antennas that could be used as a fuzing antenna. We have summarized antenna performance parameters, and we have shown how to process the antenna measurement data. Two copies of a reflector IRA were built, along with an integrated balun. Measurements were made using either a single antenna with a large reflector, or with two identical facing antennas. Good agreement with theory was achieved, and it was determined that cable loss was a significant factor that would have to be carefully considered in future measurements. We achieved a step response for the IRA with a Full Width Half Max of 36 ps, which was quite a bit faster than we set out to achieve.

Also considered here were some preliminary considerations for calculating propagation losses through frequency dependent dielectric materials. Both analytic and numerical methods were considered. Finally, we outlined how one might measure the material properties of various materials.

Acknowledgment

We wish to thank Dr. Kwang Min of Wright Laboratory / MNMF for providing funding and encouragement for this work. We also wish to thank Dr. Carl E. Baum for helpful discussions and suggestions.

REFERENCES

1. C. E. Baum and E. G. Farr, " Impulse Radiating Antennas," pp. 139-147 in H. L. Bertoni et al (eds.), *Ultra Wideband/Short-Pulse Electromagnetics*, Plenum Press, New York, 1993.

2. E. G. Farr, C. E. Baum and C. J. Buchenauer, "Impulse Radiating Antennas, Part 2," to be published in H. L. Bertoni et al (eds.), *Ultra Wideband/Short-Pulse Electromagnetics, Part II*, Plenum Press, New York, 1994.

3. E. G. Farr and C. E. Baum, Prepulse Associated with the TEM Feed of an Impulse Radiating Antenna, Sensor and Simulation Note 337, March 1992.

4. E. G. Farr and C. J. Buchenauer, Experimental Validation of IRA Models, Sensor and Simulation Note 364, January 1994.

5. C. E. Baum, General Properties of Antennas, Sensor and Simulation Note 330, July 1991.

6. C. E. Baum, Configurations of TEM Feed for an IRA, Sensor and Simulation Note 327, April 1991.

7. E. G. Farr and C. E. Baum, The Radiation Pattern of Reflector Impulse Radiating Antennas: Early-Time Response, Sensor and Simulation Note 358, June 1993.

8. K. Kunz and R. Luebbers, *The Finite Difference Time Domain Method for Electromagnetics*, CRC Press, 1993, Chapter 8.

9. C. L. Longmire and H. J. Longly, Time Domain Treatment of Media with Frequency-Dependent Electrical Parameters, DNA Report DNA 3167F, September 1973. Also appears as Theoretical Note 113**,** March 1971, and Mission Research Corp. Tech. Rep. MRC-N-1.

10. R. Luebbers, et al, "FDTD Calculation of Scattering from Frequency-Dependent Materials," *IEEE Trans. Antennas and Propagation*, Vol. 41, No. 9, September 1993, pp. 1249-1257.

11. Fellner-Feldegg, Hugo, The Measurement of Dielectrics in the Time Domain, *The Journal of Physical Chemistry*, Vol. 73, March 1969, pp. 616-623.

12. A. Papoulis, *The Fourier Transform and its Applications*, McGraw-Hill Book Company, Inc, 1962, pp. 105-106.

13. E. G. Farr, Optimizing the Feed Impedance of Impulse Radiating Antennas, Part I: Reflector IRAs, Sensor and Simulation Note 354, January 1993.